Physics of the tumor vasculature: Theory and experiment

Heiko Rieger, Thierry Fredrich and Michael Welter

Società Italiana di Fisica

Springer

Review

Physics of the tumor vasculature: Theory and experiment[*,**]

Heiko Rieger[a], Thierry Fredrich[b], and Michael Welter[c]

Theoretical Physics, Saarland University, 66123 Saarbrücken, Germany

Abstract. Growing solid tumors recruit the blood vessel network of the host tissue for nutrient supply, continuous growth and gain of metastatic potential. Consequently the tumor vasculature has been a major target of anti cancer therapies since four decades. The main underlying strategic concepts range from "starving a tumor to death" over "blood vessel normalization" to "blood vessel growth promotion" for improved drug delivery and oxygenation for increased success rates of radiation therapy. A mechanistic understanding of the these strategies is often elusive and call for a quantitative analysis of the underlying physics. Oxygen supply as well as drug delivery is determined by blood and interstitial fluid flow, for which reason such an analysis must focus on the relation between the intra- and extra-vascular transport characteristics and the tumor vasculature morphology. Here we review the current status of theoretical concepts and computational analysis of physical determinants of the tumor vasculature and the emerging predictions for blood flow, oxygen distribution, interstitial fluid pressure and efficiency of drug delivery.

1 Introduction

The blood vessel network of living organisms circulates and transports nutrients, oxygen, carbon dioxide, hormones, and blood cells to and from the cells of the tissue. Malignant tumors recruit the existing vasculature of the host tissue for nutrient supply, continuous growth and gain of metastatic potential. Angiogenesis (the formation of new blood vessels), vessel cooption (the integration of existing blood vessels into the tumor vasculature), and vessel regression remodel the healthy vascular network into a tumor specific vasculature that is in many respects different from the hierarchically organized arterio-venous blood vessel network of the host tissue [1]. Consequently blood flow, oxygen and nutrient supply, and interstitial fluid flow have tumor specific abnormalities [2] that have dramatic consequences for anti-cancer treatment: a) tumor vasculature is highly irregular and spatially inhomogeneous comprising regions with low microvascular density (like a necrotic core) leading to severe hypoxia (deprivation from oxygen) [3] and thus impeding the effectiveness of radiation therapies [4]. b) tumor vessel walls are leaky, *i.e.* have a high permeability for blood plasma, and a functioning lymphatic drainage is absent in most malignant tumors, leading to bulk flow of free water in the interstitial space, denoted as interstitial fluid flow (IFF) [1]. The resulting elevated interstitial fluid pressure (IFP) together with low microvascular pressures may retard extravasation of molecules and concomitantly drug delivery to pathogenic cells, especially in large tumor [5–7]. Indeed high IFP is still regarded as an obstacle in cancer therapy [8,9]. Therapeutic concepts like vessel normalization via anti-angiogenic therapy have been developed [10] that actually decrease IFP and improve drug penetration in tumors [11]. Additionally the normalized tumor vasculature shows restored oxygenation and augments tumor radiation response (see [12] for a review). Recently another strategy was suggested, which even promotes tumor vessel growth and also shows drug delivery improvement in pre-clinical studies [13].
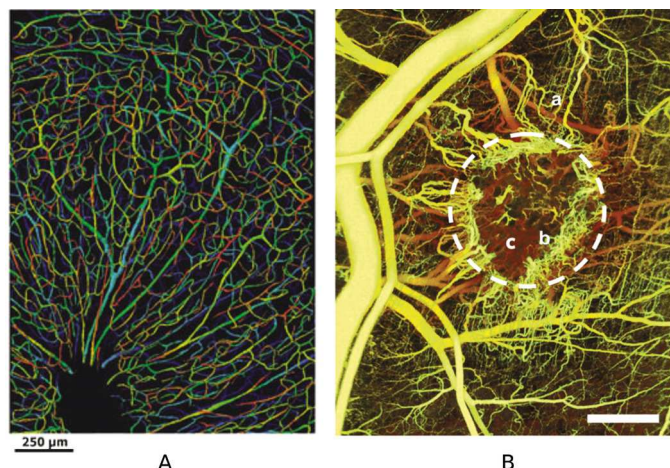

Fig. 1. Comparison of a normal vascular network with a tumor vascular network. (A) Part of a human cranial blood vessel network. A projection view of three-dimensional microscopy data is shown, color coded by depth. (Reprinted from [42], fig. 4a, with permission, © 2006, Taylor & Francis LLC.) (B) Blood vessel network of a mouse, bearing a mammary carcinoma (tumor location indicated by dashed circle). The network exhibits many abnormally dilated, tortuous, vessels which run toward the tumor and branch strongly (a). The tumor edge is densely vascularized. However, the vessel density drops off rapidly a short distance into the tumor, the interior of which appears almost void of vessels (c, b; scale bar = 1 mm; reprinted from [134], fig. 1B, with permission. © 2011, James W. Baish *et al.*)

A mechanistic understanding of these strategies is still lacking and calls for a quantitative analysis of the underlying physics. Drug delivery as well as oxygen supply are determined by blood and interstitial fluid flow, for which reason such an analysis must focus on the relation between the intra- and extra-vascular transport characteristics and the tumor vasculture morphology. In this paper we review the current status of theoretical concepts and computational analysis of physical determinants of the tumor vasculature and the emerging predictions for blood flow, interstitial fluid pressure and efficiency of drug delivery. It is organizes as follows: First the basic facts about the morphology of arterio-venous blood vessel networks of healthy tissues are reviewed in sect. 2, together with computational methods to create synthetic arterio-venous networks that can be used as the starting point for theoretical studies of the vascular remodeling during tumor growth. Here also the standard methods to compute blood flow and hematocrit (the concentration of red blood cells) in pipe networks are presented. In sect. 3 the most important processes involved in remodeling the vasculature during tumor growth —vessel cooption, angiogenesis, and regression— are discussed. It is sketched how these processes are integrated into theoretical models that predict morphological characteristics of the tumor vasculature and blood flow patterns including blood-borne drug transport. Interstitial fluid flow and transvascular fluid exchange is reviewed in sect. 4, together with computations of interstitial drug transport, where predictions for the variation of hydraulic permeabilities is also discussed. Section 5 is concerned with the physical determinants of oxygen distribution in tissue and computational models for oxygen distribution in tumor tissue. Section 6 summarizes the predictions obtained with the current theoretical models for tumor vascularization, presents a comparison of quantitative data between theory and experiment, and gives an outlook on potential further developments.

2 Normal, arterio-venous vasculature

In an ideal, healthy tissue, blood flows successively through large arteries, small arteries, arterioles, terminal arterioles, capillaries, postcapillary venules, venules, small veins, and large veins [14], see fig. 1a for an illustration. The arteries as well as the veins form trees in which a large parent vessel branches into two smaller daughter vessels, with a radius relation that is well approximated by Murrays law [15] relating the radius of the parent vessel r_p and the radii of the 1st and 2nd daughter vessel, r_{d1} and r_{d2}, respectively,

$$r_p^3 = r_{d1}^3 + r_{d2}^3. \tag{1}$$

Murrays law represents the solution of the optimization problem of minimum energy expenditure of the body assuming that only two energy terms contribute to the cost of maintaining blood flow in any section of any vessel: the energy required to overcome viscous drag in a fluid obeying Poiseuille's law (favoring thick vessels), and (b) the energy metabolically required to maintain the volume of blood and vessel tissue involved in the flow (favoring thin vessels). The relation (1) agrees surprisingly well with experimental measurements, giving an exponent slightly smaller than 3 (*i.e.* $r_p^\alpha = r_{d1}^\alpha + r_{d2}^\alpha$ with $\alpha \approx 2.7$–3.0, [16]).

The hierarchical organization the normal vasculature with branchings that follow closely Murrays law has consequences for the radius dependence of various blood flow quantities in each tree (arterial and venous) separately:

– Arterial blood pressure increases with increasing radius from ca. 30 mmHg at $r = 4\,\mu$m to ca. 80 mmHg at $r = 25\,\mu$m, and venous blood pressure decreases with increasing radius from ca. 30 mmHg at $r = 4\,\mu$m to ca. 20 mmHg at $r = 25\,\mu$m, measured in cat mesentery [1].

– Blood velocity (to be precise: maximum red blood cell velocity) increases with radius in both trees, from ca. 7 mm/s at $r = 5\,\mu$m to ca. 25 mm/s at $r = 25\,\mu$m in arterioles and from ca. 2 mm/s at $r = 4\,\mu$m to ca. 8 mm/s at $r = 25\,\mu$m in venules, measured in rat and mouse cranial windows [17]. Blood flow velocity in human capillaries is approximately 0.3 mm/s ([18], p. 712).

– Pressure gradient decreases with increasing radius in both trees [1].

The relation between vessel radius and red blood cell velocity is approximately linear, which is plausible for vascular trees obeying Murrays law (with exponent 3) since total blood flow has to be conserved between consecutive levels of the hierarchical tree.

Grouping together all arteries of the same level and also all veins of the same level one observes that the total vessel surface area in each group increases dramatically with increasing level number, *i.e.* with decreasing radius [16]. Consequently the large surface area of the highest level vessels, the capillaries, together with their structure (lack of a smooth muscle cell coat) make them the ideal site for the exchange of material between the blood and tissues. The microvascular density (MVD), given by the average inter-capillary distance, is adopted to the nutrient and oxygen demand of the surrounding tissue. In well-vascularized tissue the average inter-capillary distance is 50–100 μm, in highly vascularized tissue like brain even less, depending on the oxygen demand and the resulting diffusion length.

2.1 Mathematical representation of the normal vasculature

In early models of angiogenesis, the initial network consisted only of a single parent vessel [19]. These models adequately describe angiogenesis in the rabbit eye model [20]. Essentially, a small tumor on the cornea of the rabbit eye stimulates vascular sprouting in a few large parent vessels from up to 1 mm away. These sprouts branch excessively and form a dense capillary mesh between the tumor and the parent vessels. Similar configurations were used in later work [21–24]. However, in the bulk of tissue, the distance to sites of angiogenic activity is evidently only a few hundred micrometers [25, 26]. Therefore, the capillary plexus of normal tissue is often represented by vessel segments arranged in regular patterns, *e.g.* as square grid, or hexagonal grid, omitting supplying arteries and draining veins [23, 27–34]. Blood flow is computed assuming a fixed blood pressure at boundaries of the simulation box. Other authors use random arrangements of lines *e.g.* [35] or Voronoi cells as basis for vascular networks [36].

Two decades ago, algorithmic construction of arterial trees was already considered by Schreiner *et al.* [37]. The basic idea of this algorithm is to grow a tree, branch by branch. At each step, the existing tree is first geometrically scaled to increase in dimension. This increases the distance between vessels, implying that tissue oxygenation would worsen each step. However a new segment is added according to some optimality criterion in order to supply the voxel in space that is most in need of oxygen. Thus, oxygenation stays approximately constant. This process is repeated until the desired size is reached. Later Gödde and Kurz [38] developed a lattice based growth model which represents the entire connected vessel network including arteries, capillaries and veins so that blood can flow. This model was adopted in [39–41] with shear-stress based vascular remodeling. The construction steps are sketched in fig. 2: First, random arterial and venous trees are grown by successive attachment of new bifurcations at existing tree leafs. Then connections, representing capillaries, are added between leafs of the arterial and venous trees to allow for computation of blood flow. In a following iterative process, vessels exhibiting low shear stress are pruned while leafs exhibiting high shear stress are allowed to grow. This way, interdigitating trees develop until eventually the vasculature converges to a (mostly) stationary configuration. Implementation is given in ref. [41].

In future it might be possible to obtain real scanned blood vessel networks of sufficient accuracy and size. However, current state of the art microscopy methods can only see through a tissue slab up to a maximal depth of ca. 250 μm [42], see fig. 1a, for an example. Recently, data obtained from micro computed tomography (μ-CT) was used by Stamatelos *et al.* [43] to reconstruct large parts of the vascular system of an animal-model breast tumor. However, it is questionable if all capillaries were captured since the resolution of the scanner was only 8 μm, and many dead ends were in the reconstructed network. Similar results were obtained for other cranial [44] and coronary [45] blood vessel networks.
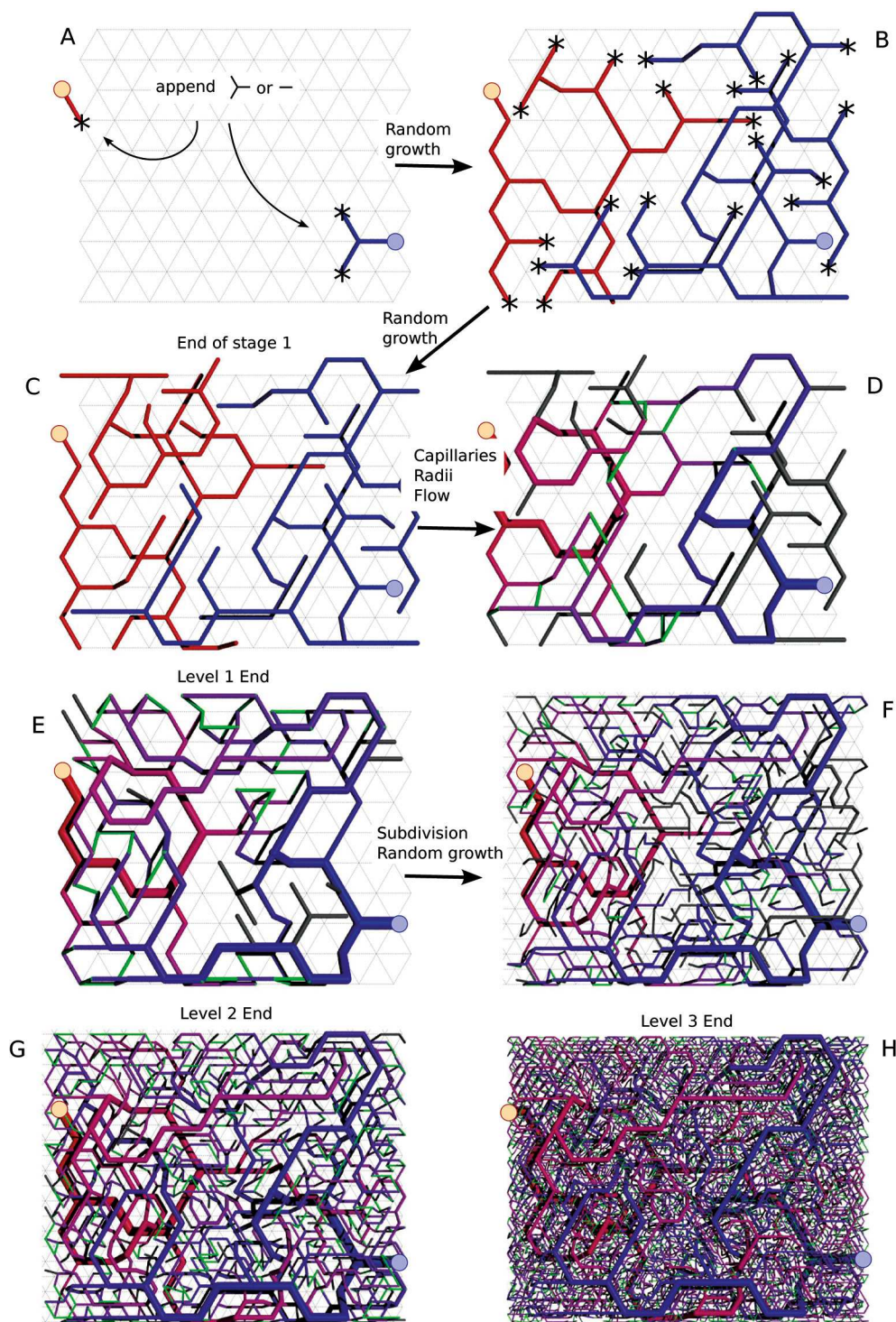
Fig. 2. Sketch of the vessel network generation algorithm. The background mesh depicts the $z = 0$ layer of a lattice with $10 \times 10 \times 2$ sites. Vessels depicted as color coded cylinders (red = arterial; blue = venous, green = capillaries). If available (D to H), the color varies in proportion to blood pressure. The algorithm is initialized with some root nodes (circles in A-H). (A) shows the state after two growth iterations. Stars indicate the open ends where further elements can be appended. (B) shows the state during the random growth process. (C) shows the state at the end of the random growth process. Further additions would cause overlap which is forbidden. In (D) capillaries were added, radii computed and blood flow computed. Unperfused branches are displayed in dark gray. Capillaries are green. (E) displays the state after shear-stress based remodeling. (F) shows the network on a lattice which was upscaled once, doubling the number of sites and the length of the original vessel segments to span over two lattice bonds. Previous tips served as starting points for random growth as in A to C. This was followed by determination of radii, generation of capillaries, and computation of blood flow as in C to D. (G) shows the result from (F) after remodeling. Here perfused capillaries are well distributed. (H) shows the final state after an additional up-scaling step. (Reprinted from [40]; © 2013, Welter and Rieger.)

2.2 Computation of blood flow and hematocrit

Depending on the application, blood flow can be considered on various scales, *i.e.* from computation of the velocity field on micrometer scale to bulk perfusion measured in ml blood ml tissue^{-1} min^{-1} as *e.g.* obtained from positron emission tomography (PET). For pipe networks of tumors models, blood flow is approximated as ideal laminar flow, where the flow rates q define the blood volume throughput per time through each pipe. Blood pressure variables, p, are associated with nodes. Thus, q is determined by Poiseuille's law

$$q = \frac{\pi r^4}{8\eta} \frac{\Delta p}{l} \,, \tag{2}$$

where r is the vessel radius, η the viscosity, l the length, and Δp denotes the blood pressure difference between the ends of the segment. Conservation of mass requires that the flow into a node equals the flow out of the node, *i.e.*

$$\sum_i q_i = 0, \tag{3}$$

analogous to Kirchoff's laws of electricity, where i indexes vessels adjacent to a given node under consideration. Together with boundary conditions, a system of equations is obtained which is sparse and can be solved with standard numerical methods, *e.g.* using a sparse LU-factorization of the corresponding system matrix. Because of the red blood cell (RBC) content, blood is a non-Newtonian fluid, *i.e.* its viscosity $\eta(r, H)$ depends on the vessel radius r and on blood hematocrit H, which is known as Fahraeus-Lindqvist effect. The hematocrit is the blood volume fraction of RBCs. Therefore, the viscosity is commonly expressed by the decomposition into the product of the blood plasma viscosity η_{plasma}, which is constant, and a correction factor, the relative viscosity $\eta_{rel}(r, H)$. Pries *et al.* [46, 47] derived a well-known phenomenological formula for $\eta_{rel}(r, H)$, which is easy to implement. However, the determination of the hematocrit H distribution is non-trivial. Note that the dependence of the viscosity on the radius varies only by a factor of 5 in the range from $r = 4$ to $r = 25\,\mu$m and is therefore weak as compared to the radius dependence of the flow which is proportional to r^4.

Blood viscosity and oxygen content depend on hematocrit, which has therefore to be take into account. Two well known effects contribute to the uneven distribution of hematocrit [48]. First, the Fahraeus effect, where the hematocrit in a small perfused tube is lower than the hematocrit at the inlet. This is due to the formation of a RBC-free boundary layer, so that RBCs in a central RBC rich core travel faster than the average blood velocity. The second effect is the phase separation effect where RBCs at arterial bifurcations prefer to flow into either of the branches depending on blood flow rates and geometry. Again a phenomenological formula was constructed that describes the phase separation effect at a junction based on *in vivo* measurements [48]. It yields the down stream RBC flow in one down stream vessel at a bifurcation as a function of the upstream hematocrit and the radius and blood flow of downstream and upstream vessels. This relation holds for arterial bifurcations, at venous junctions the downstream hematocrit is determined by mass conservation alone since only the hematocrit in one downstream vessel is unknown. Since blood flow depends on hematocrit and hematocrit distribution at bifurcations depends on blood flow one conveniently uses iteration schemes [49] until convergence to a self-consistent solution, usually in a few iterations [50], see also [32, 41].

3 Tumor vasculature

Tumor vasculature, the blood vessel network supplying a growing tumor with nutrients like oxygen or glucose, is in many respects different from the hierarchically organized arterio-venous blood vessel network in normal tissues [1]. In order to grow beyond a size of approximately 1–2 mm^3 the tumor has to switch to an angiogenic phenotype and to induce the development of new blood vessels mainly via sprouting angiogenesis, *i.e.* the formation of new vessels from pre-existing vasculature [51, 52]. This process is regulated by a variety of pro- and anti-angiogenic factors and as a consequence the anatomy of a solid, vascularized tumor grown within in a vascularized tissue displays a characteristic compartmentalization into essentially three regions [25, 26, 53, 54]: i) The highly vascularized tumor perimeter with a microvascular density (MVD) that is substantially higher than the MVD of the surrounding normal tissue. ii) The well vascularized tumor periphery with dilated blood vessels and a tortuous vessel network topology. iii) A poorly vascularized tumor center with large necrotic regions threaded by only a few very thick vessels that are surrounded by a cuff of viable tumor cells. Figure 3 shows histological sections of growing rat glioma brain tumors demonstrating the emerging compartmentalization of the tumor vasculature.

Several microscopic phenomena on the cellular level have been identified to be involved in this remodeling process: 1) Angiogenic sprouting: Up-regulation of pro-angiogenic factors in tumor-cells (like vascular endothelial growth factor, VEGF, and other growth factors) can create additional vessels via sprouting angiogenesis in some regions of the tumor, most frequently in its perimeter [51, 52]. 2) Vessel regression: The maintenance of incorporated mature microvessels
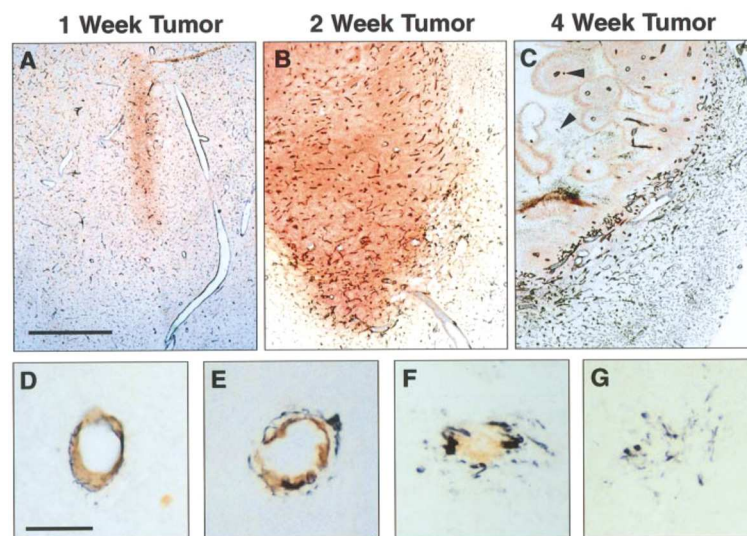
Fig. 3. Histological sections of rat glioma brain tumors. (A-C) depict the progression of a tumor (viable tumor cells stained red; endothelial cells stained black; scale bar = 1 mm). Small 1-week tumors exhibit normal appearing blood vessels. After two weeks, decreased density and vaso-dilation are visible. In 4-week tumors, vessels are mostly isolated and have cuffs of viable tumor cells around them. Distal regions are necrotic. The tumor rim is densely vascularized. (D-G) depicts regression of a blood vessel with detachment of pericytes and smooth muscle cells (black) from the vessel wall (brown). (Scale bar = 50 μm; reprinted from [26] with permission. © 2005, American Association for the Advancement of Science.)

depends on the survival of endothelial cells (ECs) and their survival is intimately tied to their local microenvironment and, in particular, to the presence of pericytes, survival promoting cytokines, and extracellular matrix proteins. The major molecular players that control this process are angiopoietins and VEGF [26, 53], and in coopted blood vessels Ang-2 is up-regulated, causing the destabilization of their capillary walls, *i.e.* the detachment of pericytes from the endothelial tube. Once ECs are separated from pericytes, they become particularly vulnerable resulting in the regression of destabilized vessels, cf. fig. 3. 3) Vessel dilation: The vascularization program of the pro-angiogenic phenotype can be switched from sprouting angiogenesis to circumferential growth in the interior of the tumor. This switch is mediated by the guidance molecules EphB4 (and its ligand ephrinB2), both expressed by ECs of malignant brain tumors [55], which acts as a negative regulator of blood vessel branching and vascular network formation, and also reduces the permeability of the tumor vascular system via activation of the Ang-1/Tie-2 systems at the endothelium/pericyte interface.

Besides pro- and anti-angiogenic molecular factors physical determinants like mechanical, hydrodynamical and collective processes are involved in the transformation or remodeling of the original arterio-venous blood vessel network into a tumor specific vasculature. As for the generation of vascular networks in organ development a complex interplay between chemical signals, guidance proteins, and mechanical forces determines the morphology and the function of the the emerging tumor vasculature. A recent comprehensive reviews either on mathematical models for the formation and remodeling of vascular networks can be found in [56] and a systems biology view on blood vessel growth and remodeling is given in [57].

3.1 A model for vascular remodeling

Earlier work focusing on tumor induced angiogenesis can roughly be divided into three categories: 1) continuum models without a proper representation of a blood vessel network and blood flow (see *e.g.* [58–60], 2) hybrid models with a fixed vessel network geometry and a dynamically evolving tumor (see, *e.g.* [27, 31, 61]), and 3) hybrid models with a fixed tumor (as a source of a diffusing growth factor) and a dynamically evolving tumor vasculature starting from a single parent vessel far away from the growth factor source (inspired by the original work of Anderson and Chaplain [19], see *e.g.* [23, 24, 62–65]). The latter models are also denoted as vessel-ingrowth models since the whole tumor vasculature grows from outside towards the tumor surface, a setup motivated by VEGF experiments in the rabbit eye cornea [66].

Blood vessel network remodeling during tumor growth transforms the hierarchically structured initial network of healthy tissue into a tumor specific vasculature and involves several processes: angiogenesis, vessel dilation, vessel wall degeneration and vessel collapse, as sketched in the preceding subsection. Besides angiogenesis also vasculogenesis, vasculogenic mimicry and intussusception can also contribute to the formation of new blood vessels, but appear to
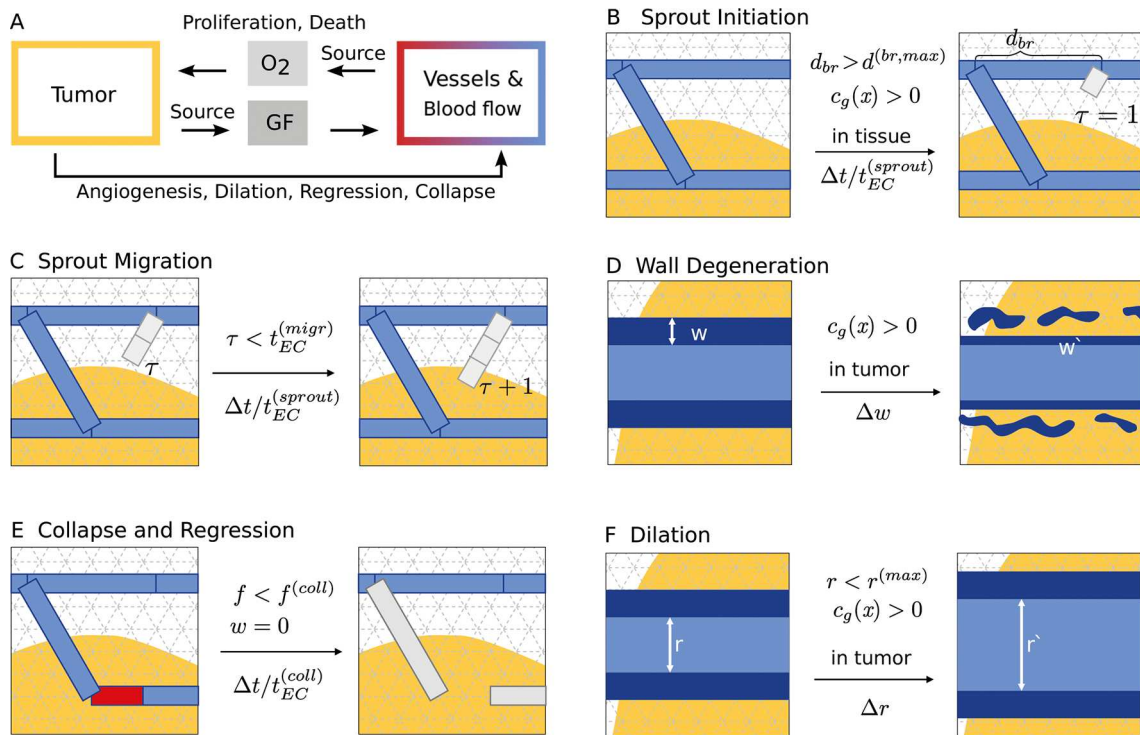
Fig. 4. Model of tumor vascular network remodeling. Following [32], tumor and vascular network interact via concentration distributions of growthfactors (GF) and oxygen (O_2), where tumor cells are sources of GF and the vascular network is the source of O_2. Blood flow is (re)computed after alterations of the vascular network to reflect the changes in blood pressure, flow rates and shear stresses (illustrated in A). Tumor cells can proliferate in response to a sufficient O_2 supply, and will die to O_2 deprivation. The dynamical processes of network remodeling are illustrated in (B-F), showing the state of vessel segments (blue) before (left) and after (right) the respective transition. Preconditions are indicated above the center arrows, and transition probabilities are denoted below, respectively. (B) depicts the start of a new sprout. A preexisting segment is split at the branching point. In general, the path length on the network to the next branching point d_{br} must be smaller than the upper limit $d^{(br,max)}$. Moreover, a sufficient GF concentration c_g must be present. The new segment is initialized with an associated life-time of $\tau = 1$. (C) depicts the further extension of the sprout from (B). Additional segments inherit τ from the parent segment. Moreover τ is incremented, globally, for all sprouts once per time step. (D) depicts the degradation of vessel walls. The variable w represents the stability of the vessel wall, here depicted as varying wall thickness. It decreases continuously according to the rate Δw, resulting in a value of w' at the next time step. In (E) an unstable vessel (red) is removed, representing occlusion of blood flow and complete disintegration. Such event is assumed to happen only to vessels with maximally degenerate walls and low wall shear-stresses f, where $f < f^{(coll)}$. The emerging dead ends trivially have $f < f^{(coll)}$, and therefore collapse rapidly, resulting in a long ranged effect. (F) depicts the dilation of tumor vessels. Their radii increase with rate Δr up to the upper limit $r^{(max)}$.

be less relevant [52]. In addition to the latter the tumor coopts the already existing vasculature and often destroys much of it, which has dramatic consequences for network morphology, blood and interstitial fluid flow patterns and drug delivery. In the following we summarize the computational model developed in [39, 40, 67] for the remodeling of an initial arterio-venous blood vessel network by a growing tumor, see also fig. 4.

Growing tumor: A mathematical representation of an growing tumor could be as simple as a linearly expanding spherical region with physiological parameters different from the embedding tissue. Physiologically realistic representations involve cell proliferation and death, cellular motility via chemo-, hapto- and mechanotaxis, cell-cell adhesion, and possibly visco-elastic and compressibility properties. A comprehensive review on continuum models for avascular tumor growth can be found in [68].

Sprout generation: VEGF stimulates endothelial cells (EC) to proliferate and migrate. The initial event is the formation of a sprout made of one or two ECs of a specialized phenotype (tip cells) that starts to migrate into the extracellular matrix (ECM). A common modeling approach [39, 40, 67] is to substitute the effect of the complex biochemical pathway involving pro- and anti-angiogenic factors leading to a sprouting event by a stochastic model in which sprouts emerge from existing vessels with a certain probability that depends on the local VEGF concentration, possibly also anti-angiogenic factors, tumor environment and lateral inhibition. The latter, delta-like 4 (Dll4)/notch mediated process, prevents sprouts from being initiated where another one has already been created earlier in the

neighborhood (for a modeling approach see [69]). Within solid tumors angiogenic sprouting is strongly inhibited, instead the presence of VEGF leads to circumferential growth [55], see below. Depending on the local VEGF gradient the sprout is also initiated with a preferred migration direction.

Sprout migration: The tip cell of a sprout responds to VEGF stimulation by extending filopodia and migrating towards the signal, *i.e.* the VEGF source [70]. Behind the tip cells so called stalk cells maintain the contact with the original location of sprout formation. They divide in response to VEGF by which the sprout elongates. The tip cells are further stimulated and the process repeats. Frequently one stipulates that sprout migration is biased along a VEGF gradient, but regarding the fact that the average vessel to vessel distance in healthy tissue is less than $100\,\mu$m and that sprouts produce filopodia of 10–$20\,\mu$m length in all directions a migrating sprout will hit nearby vessels with a high probability, irrespective of potential variations of the growth factor gradient, which are low anyway close to the tumor boundary, where most of the angiogenic activity takes place. Modeling has shown [39, 40, 67] that imprinting a growth direction at sprout initialization parallel to the local VEGF gradient is sufficient and that later directional correction due to VEGF gradient variations do not significantly improve target finding in dense vessel networks. In case a target vessel is not found within a certain distance (ca. $200\,\mu$m) sprouts retreat and vanish. Finally sprouts become normal vessels if the tip cells fuse with another vessel (anastomosis) such that blood can flow. Obviously blood flow has to be recomputed after such an event. Sprout initiation can also start from sprouts which emulates tip splitting as observed *in vivo* and *in vitro*.

Wall degeneration: As has been reported in [26, 53] the tumor environment degrades vessel walls by detachment and disintegration of cell layers and membranes around the vessel lumen. It can be implemented, for instance, by a parameter for each vessel segment, that reflects the vessel wall thickness for normal vessels, and continuously decreases for tumor vessels (*i.e.* vessels in contact with tumor cells) with the a given rate until zero.

Vessel collapse: Vessels inside the tumor can collapse and disintegrate completely [26, 53]. Obviously blood flow is pinched off inside a collapsed vessel, which necessitates again the recomputation of blood flow. It can be modeled as a stochastic process [39, 40, 67] where a vessel segment can be removed with a certain probability that depends on its wall degeneration parameter, blood flow shear stress, and local solid stress. Since inside the tumor wall degeneration and solid stress do not vary strongly it is the shear force dependence of the collapse probability that appears to have the most important effect on the morphology of the tumor vasculature [33].

Vessel dilation: It has been shown [55] that inside tumors VEGF stimulated angiogenic activity switches from angiogenic sprouting to circumferential growth. During circumferential growth the vessel radius increases continuously with a certain rate until maximum radius is reached or local conditions (like solid stress or flow conditions) induce dilation arrest. It should be emphasized that this process is particular important for blood flow characteristics within the tumor since the blood flow varies with the fourth power of the radius and only modest vessel radius increase by a factor of 2 or 3 has leads to an extreme increase in blood flow.

Some authors also incorporated structural adaption into their models [27, 29, 61], which means that in response to tissue needs microvascular networks are capable of inducing long-term changes of vessel diameters [71]. Based on experimental data from healthy tissues a theoretical model in dependence of various stimuli like endothelial wall shear stress, intravascular pressure, a flow-dependent metabolic stimulus, and a stimulus conducted from distal to proximal segments along vascular walls [71]. Although structural adaption might be relevant for the vascularization of the healthy tissue surrounding (and feeding) the tumor vasculature, it is not clear in how far these radius adaption mechanisms work also for tumor vessels.

3.2 Simulations of the tumor vasculature

The first studies of vascular remodeling during tumor growth assumed a simplified initial vasculature representing a capillary network arranged on a regular grid: Bartha and Rieger [32] introduced the concept of vessel cooption, regression, and dilation into models for vascularized tumor growth, which were extended from two space dimension, and studied the dynamical change of vessel network morphology in tumor growth in two space dimensions [32, 72] and in three space dimensions [33]. As a robust model prediction emerged: the characteristic compartmentalization of tumor vasculature into the highly vascularized tumor perimeter, a well vascularized tumor periphery with dilated blood vessels, a tortuous vessel network geometry, and a poorly vascularized tumor center with large necrotic regions threaded by only a few very thick vessels that are surrounded by a cuff of viable tumor cells.

The essential drawback of models assuming a grid-like initial vasculature is a global blood flow bias from one corner of the simulation box towards the opposite, imprinted by the boundary conditions for the blood pressure. Such a bias is generally absent in large physiological blood vessel networks and leads, if shear force determined vessel collapse is taken into account, to a preferential direction of inner tumor vessels [32, 33, 72]. Moreover, due to the absence of strong pressure differences between nearby vessel (as they occur between arteries and veins in realistic tumor vessel networks [73]), the formation of strongly perfused shunts is excluded, altering the expected blood and interstitial fluid flow characteristics in an unphysiological way.
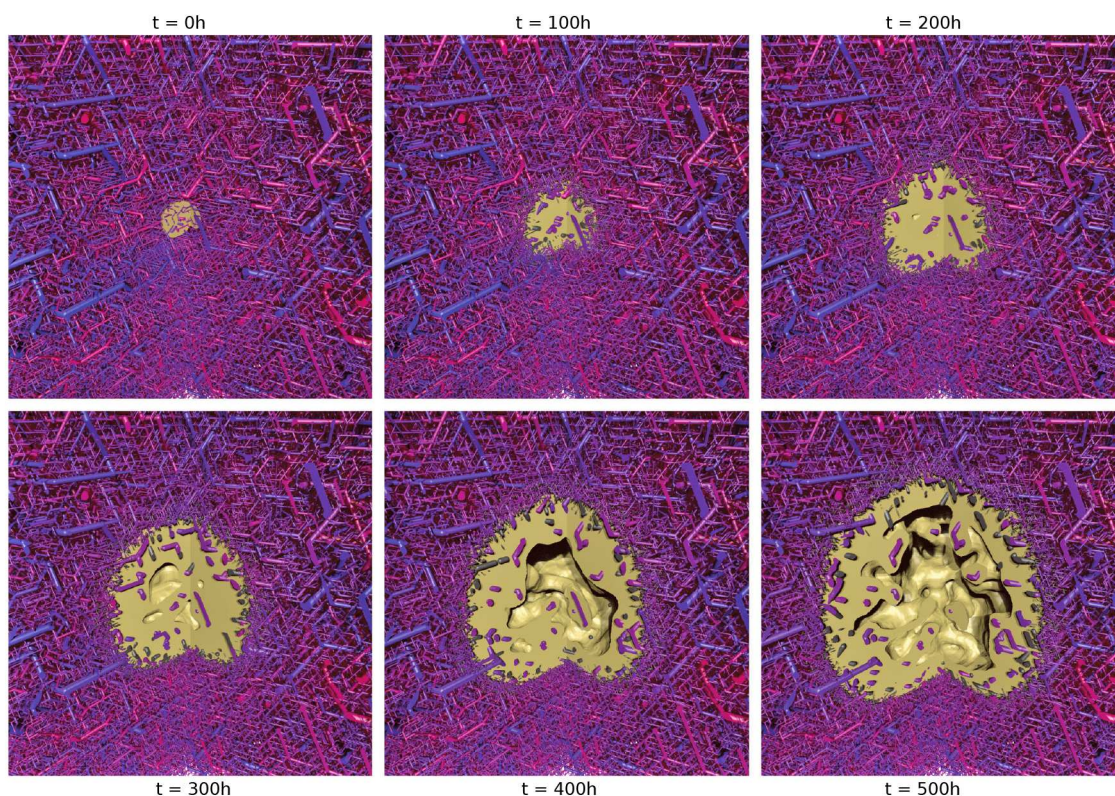
Fig. 5. Simulated tumor growth and vascular remodeling. The image sequence shows the temporal evolution of the vascular network and of the interface between viable tumor cells and normal or necrotic tissue (yellow blob). It is a three-dimensional system, computed for [40], of which a quadrant is cut out so that the tumor interior can be seen. The view is zoomed in slightly, whereas the full system can be seen in fig. 6. For scale: the tumor radius at $t = 500$ h is ca. 1.8 mm. Vessel segments are color coded by blood pressure (red is high; approximately 10 kPa, or 75 mmHg). At $t = 0$ h the simulation is initialized with a small tumor nucleus in the center and a pre-generated vasculature of the host. The oxygen consumption of tumor cells is elevated compared to normal tissue, leading to a drop of the tissue oxygen concentration, secretion of diffusing GF and stimulation of angiogenesis. As a result, at $t = 100$, the vascular density (MVD) has increased near the tumor rim. Unperfused segments, *i.e.* blind ends, are displayed in dark gray. Some of them are newly extending angiogenic sprouts. Others pertain to vessel segment chains where one segment has been removed according to the vascular regression and collapse process, pinching off blood flow. Angiogenesis, dilation and regression act mostly near the expanding tumor-tissue interface, transforming the host vasculature into a typical compartmentalized tumor network. Necrotic regions occur as a result of hypoxia. Since only viable areas are shown, necrotic regions appear as hollow interior.

These artifacts could only be avoided by using realistic arterio-venous initial networks, as was done by Welter *et al.* in [39,67]. In fig. 5 we show a sequence of tumor-vessel-configurations obtained from a computer simulation of the model sketched above and described in full detail in [40]. Figure 6 shows a typical tumor vasculature at $t = 700$ h for simulation parameters that were adopted to reproduce experimental data for melanoma [25]. Indeed the emerging tumor vasculature morphology and blood flow distribution shows displayed significant differences when compared quantitatively with tumor vasculature predicted by models using a grid like initial network. The strong influence of the initial vascular network on the tumor's growth dynamics and its long-time composition was also reported by Perfahl *et al.* [74], who used an small initial network that was derived from experimental data.

The simulations of tumor growth in arterio-venous networks exhibit high-caliber ($> 50 \, \mu$m radius) vessels protruding into the tumor which form a backbone of stable vessels in-between which thinner vessels form short and straightforward paths [39]. The flow resistance decreases proportional to $1/r^4$ with radius r and is therefore, in comparison to capillaries, extremely low in such high-caliber vessels. Therefore, in analogy to electrical networks, the blood pressure (voltage) drop across them is also low. In zero-th order approximation the blood pressure is constant, *i.e.* high-caliber vessels act like a pressure boundary condition for adjacent capillaries. Short, directed paths carry increased flow resulting in an increased wall shear stress that decreases the collapse probability of the involved vessels. The distribution of tumor vessels thus becomes dependent on initial ($t = 0$) vascular networks and is generally heterogeneous and anisotropic. Consequently the local tumor MVD (after tumor grwoth) turns out to be correlated with local blood pressure differences between vessels of the initial arterio-venous network (before tumor growth) [39]. These results suggest that different architectures of tumor vascular networks which are observed in real tumors of the same tissue, *e.g.* breast tumors [75] are to some degree the result of the layout of the micro vasculature in which the
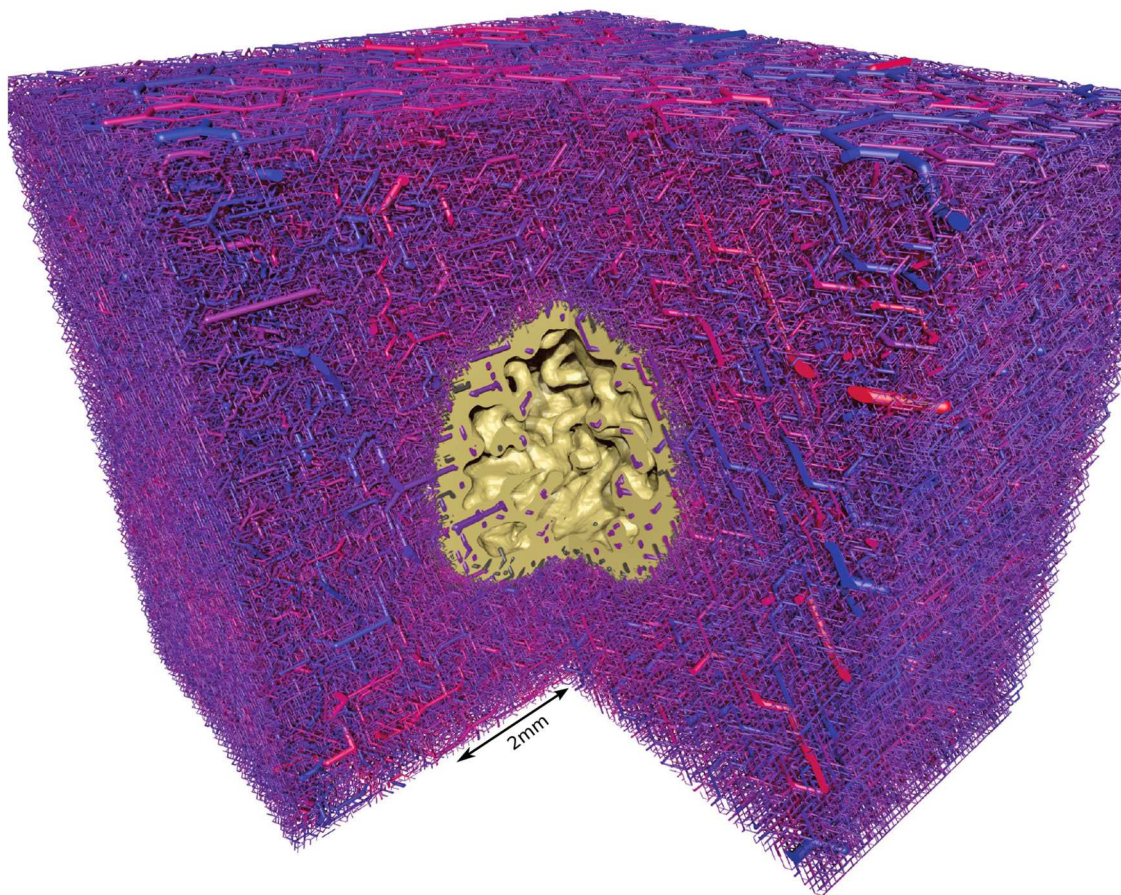
Fig. 6. Final simulated tumor and tumor blood vessel network. Depicted is a visualization of the final state of the simulation shown in fig. 5 at $t = 700$ h, where the simulation is stopped. The full simulation cube of 8 mm lateral length is shown. As before, a quadrant is cut out, the interface to viable tumor mass is shown in yellow and the vascular network is displayed as collection of cylinders, color coded according to blood pressure. The bulk of volume surrounding the (yellow) tumor spheroid is filled with the initial vascular network. It appears solid, but actually fills only ca. 10% of the available volume. The tumor vasculature exhibits the typical compartmentalization found in melanoma and glioma [26, 54] as briefly described in fig. 5. Networks such as this are the basis of further studies of interstitial fluid pressure and drug transport [40] and tumor oxygenation [41].

tumor grows, rather than caused by genetic variations within the tumor mass or by heterogeneities in the extra-cellular matrix as proposed by [76].

Furthermore, regional blood volume rBV, perfusion rBF, hemoglobin concentrations c_{Hb}, average blood oxygen saturations Y and other derived quantities were computed for a cohort of simulated tumors [41]. A significant spread of these quantities was predicted due to the selection of different initial ($t = 0$) vascular tree configurations obtained from different, arbitrary, sets of tree root locations. The origin of this spread is the variation of blood volume rBV with the number of vascular trees within the fixed simulation volume. Fewer trees require that the existing trees exhibit higher depth. Murray's law demands that each additional tree level exhibits vascular radii larger than the radii of child branches. The radii of capillaries is fixed by definition of the construction method. For these three reasons, the total vascular volume rBV increases with decreasing number of trees. Dirichlet blood pressure boundary conditions imply a corresponding variation of blood flow rBF and of all other dependent variables. Naturally, higher tree depths imply more high-caliber vessels, which implies the presence of steeper blood pressure differences in-between vessels and thus co-determines tumor vascular morphology, *e.g.* the local MVD.

3.3 Blood-borne drug transport

After injection of a drug into a main artery it will be transported with the blood flow downstream and then extravasated through the vessel walls into the interstitial space, where it is then diffusively or convectively transported and delivered to the target cells. The starting point to compute blood borne drug transport is a given configuration for the vasculature with precomputed variables for flow, flow velocity, vessel length, and radius. To follow an injected bolus of some substances during the transit through the vascular network, McDougall and Anderson [21] adopted a method from petrol engineering, originally developed to predict solute transport through porous rock. It allows the computation
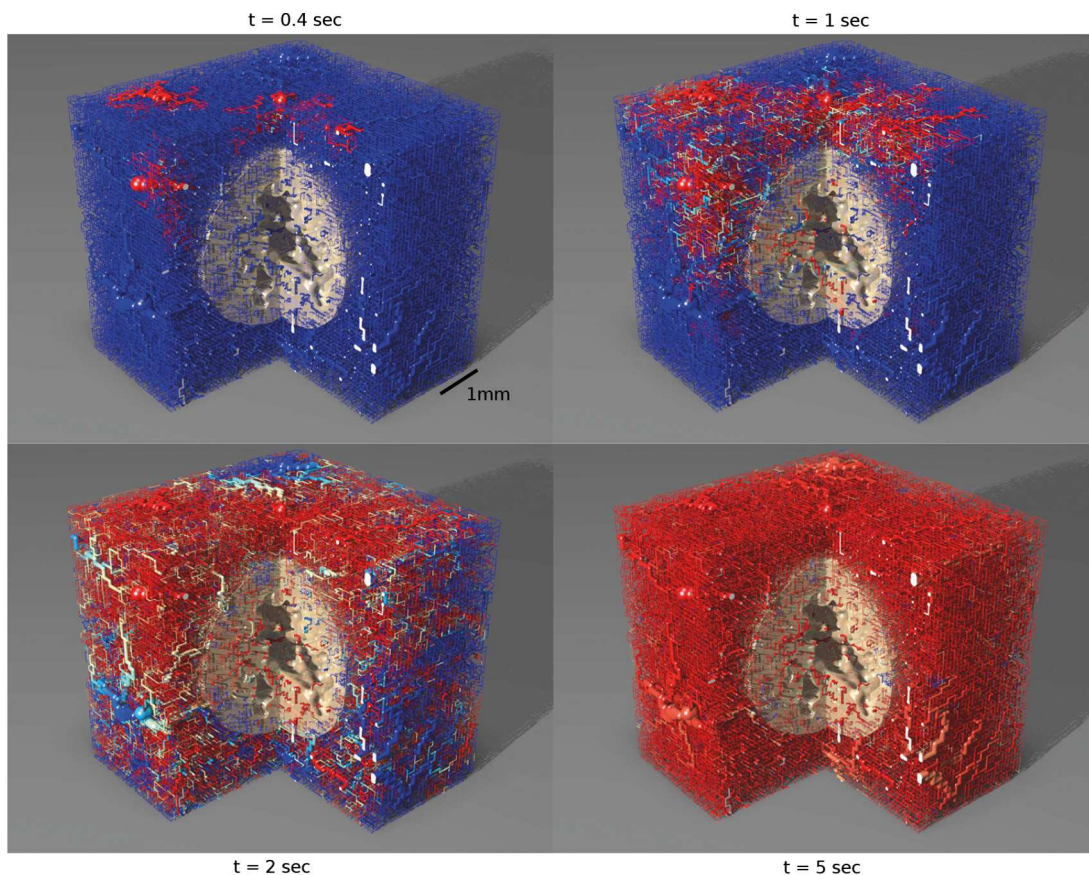
Fig. 7. Simulated conduction of an intravascular tracer. Intravascular concentrations of an inert non-extravasating tracer substance are shown at different times of a simulation. At $t = 0$ the concentration at the inlet is set to the normalized concentration 1 (red). The vasculature is initially filled with "clean" blood (blue). The width of the simulation cube is 8 mm. The vascular network is composed of vascular trees and capillaries of normal tissue and a spherical area that was remodeled by the tumor. Predicted, blood flow rates are generally high, of the order of 1 mm/s. Therefore the tracer is rapidly conducted through approximately the entire network. (Reprinted from [67] with permission; © 2010, EDP Sciences/Springer Verlag/SIF.)

of time dependent concentrations of a tracer c associated with segments of a vascular network. The basic idea is to collect amounts of tracer m in nodes of the network and distribute it downstream in proportion to the flow rates q of downstream vessels. This procedure, akin to the upwind-differencing scheme for advection equations, is applied repeatedly in time steps of length Δt. The amounts of substance from upstream vessels, added into downstream nodes, is accordingly $\Delta m = cq\Delta t$. Thus, given a time dependent inlet concentration $c_{in}(t)$, the method yields concentrations $c(t)$ of each vessel. Transvascular loss was not considered although the method would be straight forward to extend to take this into account.

The computational scheme described here was used for the simulation of blood borne drug transport in [21, 62, 63, 67, 72]. The drug flow simulations of [67] (as shown in fig. 7) using a tumor blood vessel network that emerged from an arterio-venous initial vasculature, demonstrated that drug flows relatively well through all of the networks and an infusion time of the order of a few seconds is sufficient to saturate the vasculature with drug. Therefore the model predicts that drug efficiency is not limited by the transportation process through the vasculature. Considering the model mechanisms which lead to the tumor vasculature, it is plausible that drug reaches (nearly) all parts of the vasculature: Shear force correlate vessel collapse naturally leads to elimination of weakly perfused vessels. Thus, for tumors like melanoma, which are primarily vascularized by co-option rather than vessel in-growth [25] a blood-borne "delivery problem" does not exist. This does however not automatically imply that drug reaches all tumor cells since neither drug transport through the tumor tissue nor drug uptake have been addressed [9].

4 Interstitial fluid flow

Interstitial fluid (IF) is the liquid that surrounds the cells of a tissue in a living organism and is very similar to blood plasma since both exchange continuously water, ions, and small solutes across the walls of the capillaries of the arterio-venous trees. A normal person has ca. 10 liter IF, which provides the cells of the body with nutrients and a

means of waste removal. In general the hydrostatic blood pressure pushes liquid out of the capillaries, whereas the osmotic pressure drives water back into the vessels. The lymphatic system prevents a buildup of fluid in the tissue and channels it ultimately back into the blood circulation. In healthy tissue there is a steady flow of interstitial fluid from the capillaries through the interstitial space between the tissue cells into the surrounding lymph vessels and by this interstiatial fluid flow (IFF) not only nutrients but also therapeutic drugs can be transported advectively from capillairs to tissue cells.

In tumors the lymphatic system is absent or functionally impeded, causing a significant increase in interstitial fluid pressure (IFP) [1,77] and characteristic IFF patterns, see fig. 8a. Early theoretical models assuming a spherically symmetric tumor volume with an increased homogeneous IF source strength (representing leaky vessels) and a decreased homogeneous IF sink strength (representing lacking lymphatics) indeed showed an increased IFP inside the tumor that drops sharply at the tumor boundary [6]. More realistic computations to be reviewed in the following show similar qualitative behavior.

Interstitial fluid flow (IFF) is commonly modeled as liquid flowing through a porous medium [6,23,34,65,78–81], where tissue cells and the fibers of the extracellular matrix assume the role of the medium. Fluid and medium are described in general within the framework of mixture theory with the help of distributions of their local volume fraction and their velocity distributions. However, the medium is often assumed rigid. The volume fraction of the liquid is identified with the porosity ϵ which describes the amount of space available per unit volume within the medium. This space is filled by definition with the liquid. Assuming rigidity and (quasi) stationary flow, the system is characterized by the spatial velocity field of the liquid, $v(x)$, where x is the space coordinate. The velocity v is determined by the gradient of the hydrostatic pressure p according to the well-known Darcy's Law

$$v = -K\nabla p, \tag{4}$$

where the permeability constant K is the product of an intrinsic permeability constant of the medium, the porosity and the inverse fluid viscosity. Usually, K is obtained directly from experimental data for a specific tissue type. Assuming incompressibility and constant permeability, the mass conservation equation obtained is a Poisson equation in p:

$$\nabla \cdot v = -K\nabla^2 p = Q, \tag{5}$$

where Q was added to represent sources (vessels) and drains (vessels, lymphatics). Discretization leads to a symmetric positive definite system of equations which is straight forward to solve by state of the art methods, *e.g.* FFT or preconditioned conjugate gradient [82]. In [40] this simple approach was adopted to determine IFP and IFF in vascular networks of simulated tumors. Some authors consider IFF within a fully coupled mixture model, where v is the relative velocity between the IF and a moving cell population [83]. Other authors incorporate IFF into models of tumor growth and allow compression of blood vessels due to elevated IFP [34].

4.1 Transvascular fluid exchange

Normally only a miniscule amount of blood plasma can leave the blood stream through tiny gaps between ECs. But in tumor vessels, large quantities escape through gaps where entire ECs are missing. The net loss of fluid volume per time J_v within a given control volume is given by the Starling equation

$$J_v = L_p S \left[p_v - p_i + \sigma_T (\pi_v - \pi_i) \right], \tag{6}$$

where L_p is the hydraulic permeability of the vasculature, S is the vascular surface area within the control volume, p_v is the blood pressure, p_i is the interstitial pressure, σ_T is the average osmotic reflection coefficient and π_v and π_i are the osmotic pressures of plasma and IF, respectively [6]. The osmotic term $\sigma_T(\pi_v - \pi_i)$ represents forces generated by various dissolved substances and can be considered as a constant offset from p_v at an experimentally determined value [6]. This form of transvascular coupling is straight forward to apply in models where the vasculature is considered as a homogeneous phase.

In network models of the vasculature, the flux from each individual segment has to be taken into account in eq. (5) as a local source of fluid. A simple means to facilitate this is to let the vessel network occupy the same lattice used for the numerical discretization of eq. (5) which was done in refs. [23,34,65]. Then each node of the vessel network j corresponds to a discretization site of eq. (5), and local transvascular fluxes between them can be defined according to eq. (6), where S now stands for the local surface area of the segments in the vicinity of node j. Using the standard finite difference stencil for the Laplace operator in (5) one obtains a combined system of equations, equivalent to Kirchhoff's laws. It is a common scheme in simulations of tumor growth, not limited to computation of IF, but also applied in theoretical studies of drug delivery [81,84] and oxygenation [85–89].
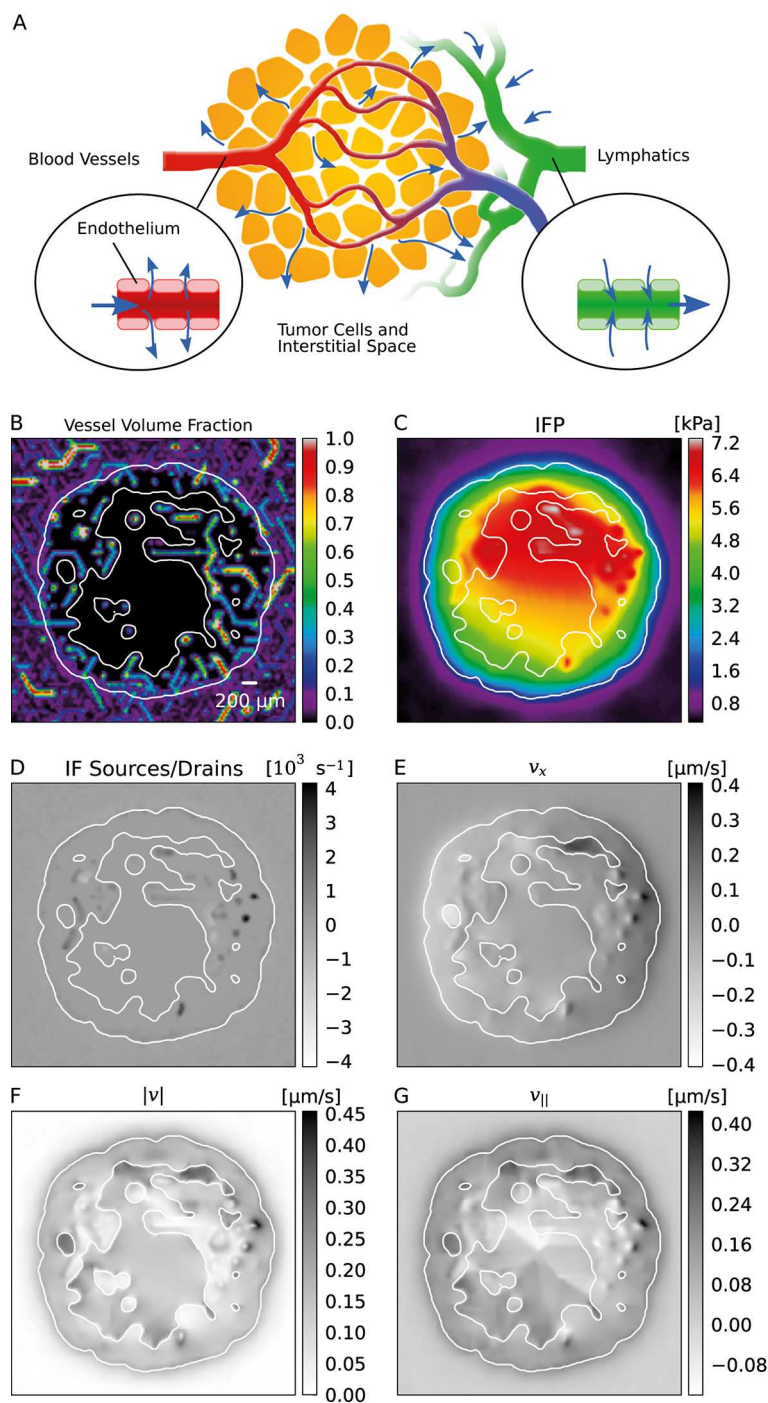
Fig. 8. Interstitial fluid flow. (A) Sketch of the transport of interstitial fluid from blood vessels through tumor tissue into lymph vessels outside the tumor. IF escapes through gaps in-between endothelial cells, which line the lumen of blood vessels, into extracellular space (left). These spaces also contain adhesion molecules and a network of fibers composed of various proteins such as collagen. Pores and fibers pose a resistance to the flow of the IF akin to the flow of water or oil through a porous rock. IF is absorbed into lymphatic channels (right) from where it is brought back into the blood stream. In normal tissue, a large resistance to transvascular flow leads to a large drop of the hydrostatic pressure across the vessel wall, so that the interstitial fluid pressure (IFP) approximately assumes the reference value of zero purported by the lymphatic system. In tumors (yellow), the IFP is elevated to approximately the level of blood pressure due to extremely large gaps in vascular walls and lack of functional lymphatics [8], 0 to 94 mmHg were measured in human tumors [78]. Cuts through three dimensional simulation data sets are shown in the remaining panels. (B) shows locations of blood vessels according to their fractional volume per simulation voxel. (C) is a map of interstitial fluid pressure. (D) shows the IF source and drain density in volume inserted per tissue volume and time. (E-G) show the x-component of the interstitial fluid velocity v, the magnitude $|v|$ and the radial component $v_{\parallel}$. The velocity is discontinuous since we assumed a $10\times$ increased permeability of necrotic regions. (B-G reprinted from [40]; © 2013, Welter and Rieger.)

More generally, vessels can be considered as line-like sources akin to the Dirac δ distribution, a concept which has been formulated mathematically rigorously for the solution of elliptic equations with Dirac terms by finite element methods [90] and applied to IFF [91]. We can thus replace (6) by the distribution

$$J(\mathbf{y}) = \int_{\Gamma} L_p 2\pi r (\tilde{p}_v - p_i) \delta(\mathbf{x} - \mathbf{y}) \mathrm{d}x \tag{7}$$

where $\mathbf{x}$, $\mathbf{y}$ are spatial coordinates on the network and in tissue space, respectively, Γ is the set of one-dimensional curves (or line segments) that describes the vascular network, $\tilde{p}_v$ is the effective blood pressure including the osmosis terms, and r is the vessel radius. The permeability L_p, blood pressure $\tilde{p}_v$ and radius r can vary depending on the position on the network $\mathbf{x}$.

4.2 Simulation of interstitial fluid flow

Welter and Rieger incorporated arterio-venous networks as sources and drains of interstitial fluid [40] into a system that was previously considered within the scope of continuum models [7, 78, 79], network models based on the rabbit-eye model [23, 24], and capillary networks [34]. Figure 8 shows color coded plots of vessel density, IFP, IF source and sink strengths and IFF velocities as predicted by the model of [40]. The model predicts an elevation of interstitial fluid pressure (IFP) to 49 mmHg within the experimentally measured range for human tumors [78], and close to the average blood pressure within the simulated tumor. A peak radial flow velocity of $0.2 \, \mu\mathrm{m/s}$ is predicted at the tumor edge, also in agreement with the literature.

It was often suggested that an elevated IFP poses a barrier to drug delivery [7–9, 34] and that a decrease in vessel wall permeability (an increase in hydraulic resistance) could possibly decrease IFP, increase IFF and concomitantly improve convective transport of therapeutic molecules [11]. However, the reason for improved drug delivery cannot simply be an increased transvascular hydrostatic pressure gradient that drives extravasation according to the Starling equation (6). Other parameters of the tumor vasculature must also change during vessel normalization. Interstitial fluid flow behaves similar to an electrical current through a chain of resistors, of which one resistor, namely leaky tumor vessel walls, is particularly small. Thus, an increase in leakiness results in an increase in IFP but also in an increase the liquid flux throughout the tumor, as predicted by the model of [40], see fig. 9 that shows the effect of the variation of various permeabilities in the tumor-vessel system, and which also contains a symbolic sketch of analogous resistor networks. The results show that a decrease of any of the permeabilities (vessel wall, tumor tissue, lymph vessel walls) will also decrease the emerging IFF.

The analysis of [40] is restricted to good perfusion, where only a negligible liquid fraction escapes in spite of leakiness. Otherwise the way through tumor tissue into lymphatics could presumably present an alternative well conducting pathway, draining downstream vessels of blood plasma, resulting in reported low flow velocities [92].

The recent theoretical work [34], using a capillary network and a sophisticated model of tumor growth that incorporates vessel compression due to IFP, comes to similar conclusions about the role of various permeabilities However, it was concluded that IFP is a barrier with little supporting numerical evidence, *i.e.* no simulation of actual drug transport was performed. Results from other work [23, 24] may not be directly applicable for human tumors since the physiologically unrealistic rabbit-eye model was considered.

4.2.1 Relation between peripheral IFF and central IFP

The simulation data of [40] can also be used to study the relation between the IFF at the tumor periphery and the plateau value of the IFP in the tumor center. Peripheral IFF of real tumors could be visualized non-invasively by using labeled particles which are injected into the blood stream. These labeled particles are extravasated from the tumor vasculature and then transported by IFF via advection to the tumor boundary into the surrounding tissue, where they could be observed with non-invasive imaging techniques. Establishing a relation between the peripheral IFF and the central IFP therefore represents a way to estimate central IFP without an invasive procedure.

In fig. 10 the results of the simulation of [40] are shown. For each realization of the tumor vasculature for fixed parameter values the peripheral IFF (pIFF) and the central IFP (cIFP) was evaluated and represented by a single point in the pIFP/cIFF diagram. For a fixed parameter set, in particular for fixed permeabilities, the points lie on a straight line, which is reminiscent of Ohm's law: voltage (representing cIFP) is proportional to current, with the proportionality constant being the resistance. One observes that a variation of the tumor tissue permeability has the strongest effect, *i.e.* changes the overall hydraulic conductivity most prominently. For the base case scenario (with tumor permeability close to the one for the surrounding healthy tissue) all other permeabilities as well as the lymph vessel density have a significant influence on the cIFP/pIFF relation. Consequently a prediction of cIFP based on the observation of pIFF is indeed possible, but only if all physiological parameters of the tumor tissue, vessel walls, lymph vessel walls and lymph vessel density, are know.
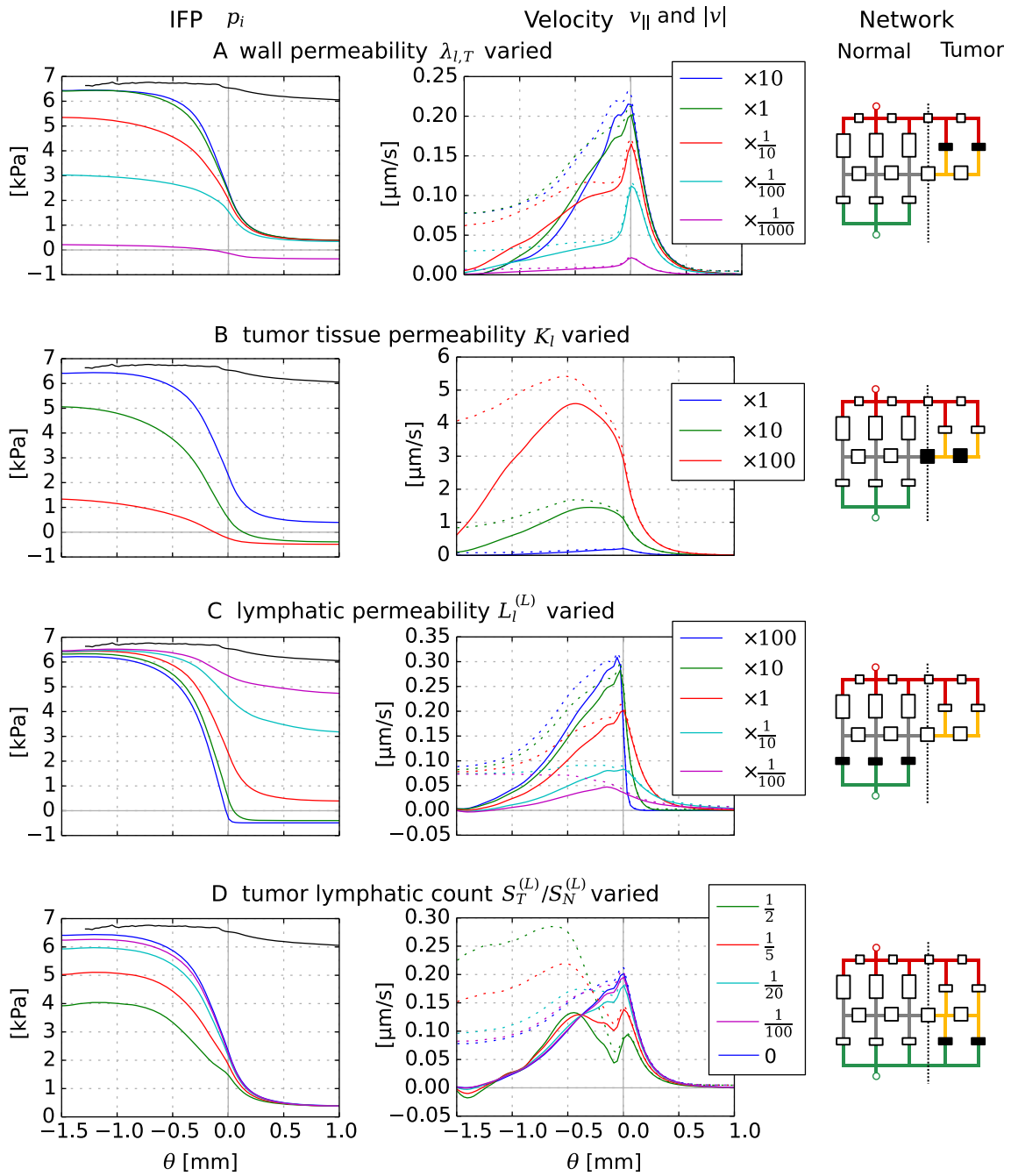
Fig. 9. Radial distributions of IFF and IFP as result of parameter variations. Left column shows the IFP and the center column shows the IFF The curves are obtained from averages over annular shells and over a cohort of 15 simulated tumors. Our model of IFF is analogous to an electrical network, where the IFP is the electrical potential. The right column shows a simplified schematic of this network, including, from top to bottom, blood vessels (red), normal interstitial space (grey), tumor (orange), and lymphatics (green). Outlined boxes represent various resistances, or permeabilities, in the system, where solid black indicates the parameter varied. The relative deviation from the original base case parameter values is given in the figure legends, except in (D). The considered cases are as indicated in the sub-figure heading: (A) Variation of the upper vessel wall permeability bound $\lambda_{l,T}$ (case iv in [40]). (B) Variation of the interstitial permeability coefficient K_l (case v in [40]). (C) Variation of the lymphatic wall permeability $L_l^{(L)}$ in normal tissue (case vi in [40]). (D) Variation of the amount of tumor lymphatics $S_T^{(L)}/S_N^{(L)}$, where the legend shows $S_T^{(L)}/S_N^{(L)}$ directly (case vii in [40]).
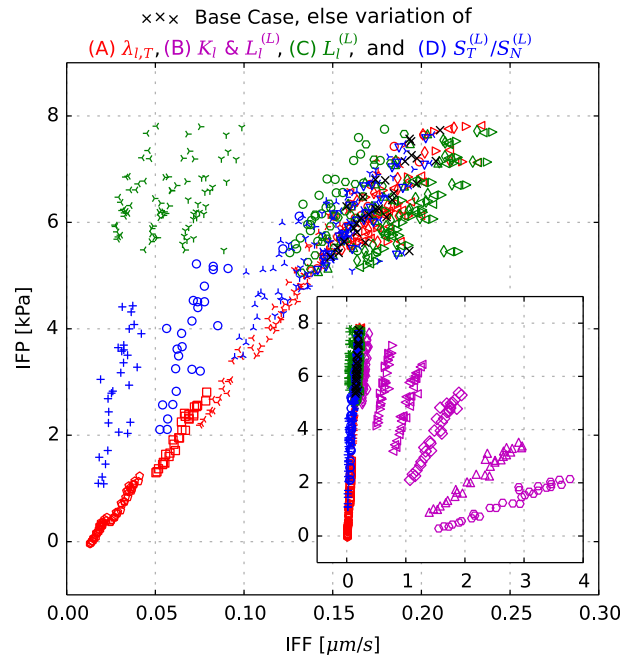
Fig. 10. Interstitial fluid flow *versus* interstitial fluid pressure. The scatter plots show data point of simulated tumors at $t = 800$, comprising data sets also used for fig. 9. The calculated IFF is the average over a $200\,\mu$m wide annular shell, centered at the tumor edge, *i.e.* reaching $100\,\mu$m into the tumor. The calculated IFP is the average over a sphere of radius $500\,\mu$m at the coordinate origin. The data comprises cohorts of tumors of different cases of parameter variations (color coded), corresponding to fig. 9. The parameters varied are (A) tumor vascular permeability $\lambda_{l,T}$, (B) interstitial and lymph permeability K_l and $L_l^{(L)}$, (C) lymphatic permeability $L_L^{(L)}$, and (D) the number of tumor lymphatics as fraction of the number of lymphatics in normal tissue $S_T^{(L)}/S_N^{(L)}$. The relative variation from the base case is coded by the marker symbols as follows: $\bigcirc = 100$, $\triangle = 50$, $\diamondsuit = 20$, $\triangleleft = 10$, $\triangleright = 5$, $\diamondsuit = 2$, $+ = 1$, $\times =$ Base Case, $\bigcirc = 1/2$, $\lambda = 1/5$, $Y = 1/10$, $\succ = 1/20$, $\nabla = 1/50$, $\prec = 1/100$, $\square = 1/200$, $\ominus = 1/500$, $\ominus = 1/1000$. In the main plot, case (B) was left out to better show the other data.

4.3 Simulation of interstitial drug transport

In order to shed light on barrier to drug delivery, transport through tissue by advection and diffusion after extravasation must be taken into account. For this purpose, Welter and Rieger analyzed a simple model, according to which, we computed time-dependent concentration distributions of drug in simulated tissues containing a vascularized tumor, grown in three-dimensional AVNs [40]. The considered tumors were static, and obtained by simulations guided by melanoma and glioma. In addition to concentration distributions, we also computed time-integrated local doses as time-independent metrics of drug delivery. The base case is guided by data for Doxorubicin [84, 93, 94], and many more cases and parameter variations were explored. Experimentally, the spatio-temporal distribution of drugs has not been studied much due to the lack of suitable markers for direct observation. Doxorubicin concentration distributions were observed exploiting auto fluorescence. Predictions of our model are in fair agreement with the above references. However, quantitative data are hardly available.

The model predicts that, in general, the dose delivered is subject to a compartmentalization similar to the vascular density (MVD). For the base case and most other cases, the average dose within the center of the tumor spheroid is significantly lower than in normal tissue, and doses are highest at the tumor edge. This result provides an additional explanation of the incompletely understood success of combination therapies of anti-angiogenic agents and chemotherapy, whereas a single drug fails to improve survival [95]. TCs behind the tumor edge might be killed by high doses of chemotherapeutics, effective against cycling cells, whereas the TC population of the tumor center is reduced by necrosis caused by hypoxia. A monotherapy might leave the one or the other part of the TC population unaffected. The mechanism by which combination therapies are known to act is suppression of the activity caused by vascular growth factors, leading to a decreased vascular permeability. This allows throughout better delivery of chemotherapeutics due to improved perfusion [95].

Variation of the various permeabilities shows that average doses delivered increase in differing sensitivity with the permeability, see fig. 10. Doses showed the highest sensitivity with respect to interstitial hydraulic and diffusive permeabilities which were varied simultaneously. As already suggested in experimental [96–98] and theoretical [99] studies this could be exploited for therapy, however care must be taken to not accidentally aggravate tumor invasiveness [100] or metastatic shedding of TCs. Moreover, angiogenic normalization therapy, *i.e.* a reduction of permeability and pruning of superfluous vessels [95], might be ineffective or even detrimental for tumors where blood flow is negligibly impaired.

Doxorubicin molecules have a molar mass of $543\,\mathrm{g/mol}$. This and lighter molecules have the advantage that diffusion helps to distribute a substantial dose homogeneously around blood vessels. Recent simulations of another group [84] predicted very smooth and homogeneous concentration distributions of the more diffusive drug Cisplatin ($300\,\mathrm{g/mol}$) arising from extravasation from a capillary-only network. Since the diffusion coefficient decreases with the molar mass of the solute, transport of drugs like nano-particles is strongly advection dominated. Such a case was considered previously with the help of a simple one-dimensional continuum model, predicting that hardly any drug is released by the vascular network into the tumor center [7]. Our model predicts interstitial drug concentrations that follow the stream of interstitial fluid in significant concentrations through the largest parts of the tumor spheroid, starting from the initial insertion through the vasculature. However, simulations frequently yielded small isolated islands behind the tumor edge where no noteworthy dose had been delivered within the time frame of the simulation of 96 h. Presumably, this discrepancy to earlier work [7] is caused by the discrete nature of the blood vessel network allowing for flow in-between vessel of different blood pressure levels. However the radial flow component vanishes by chance at some places as dictated by the random layout of the vascular network. Thus locations further outwards are hardly supplied with drug [40]. This suggests that a mono-therapy with agents of high molar mass would be prone to recurring cancer.

5 Oxygen distribution

Oxygenation of tissues has been studied in great detail theoretically [101, 102], beginning with the work of Krogh [103] who conceived a simple model of muscle tissue that is reduced to a central straight capillary and an outer concentric cylinder representing muscle fibers. Recent refined versions of such one-capillary models achieve very good agreement with experimental studies of artificial capillaries [101, 104–106]. The cylinder model adequately describes muscle fibers where capillaries run mostly in parallel, but many tissues such as tumors have more complex vasculatures. Further development of theoretical models to take this into account, can be roughly divided into two approaches. Some authors [41, 107–115] seek self-consistent solutions of the equations for advection of oxygen in blood within a realistic blood vessel network and diffusion of oxygen in tissue. This includes acquisition of networks either by artificial construction or experiments, as well as computation of blood flow. On the other hand, many authors use simplified models, where capillaries constitute sources of oxygen of an a-priori determined strength corresponding to a certain intravascular oxygen concentration. Depending on the application it is adequate to model the vasculature as disjoint set of points (in 2d) or lines (in 3d) that are placed in the tissue domain according to some statistical distribution or scanned images [85–89]. Thus only a stationary diffusion equation needs to be solved to determine the tissue oxygen concentration distribution. See [41] for a more comprehensive review.

For the study of intravascular oxygen transport it is crucial to take into account that oxygen is, for the most part, bound to hemoglobin in red blood cells (RBCs). Each of the four heme groups of the hemoglobin molecule can bind one oxygen molecule. The steady state of the binding and unbinding processes is described in good approximation by the Hill-curve [102]

$$S(P) = \frac{P^n}{P^n + P_{50}^n}\,, \tag{8}$$

where P is the partial pressure of oxygen, $S(P)$ is the fraction of oxygen bound relative to the maximal capacity, n is the Hill exponent and P_{50} denotes the partial pressure of oxygen where $S(P_{50}) = 1/2$. Hence, the total concentration of oxygen c is given by

$$c = \alpha P + Hc_0 S(P), \tag{9}$$

where H is the hematocrit, c_0 is the concentration of oxygen in RBCs at full saturation, and $\alpha = \alpha_p + H\alpha_{rbc}$ is the effective solubility in blood and α_p and α_{rbc} are the solubility in plasma and RBCs, respectively. The transvascular flux density j_{tv} of oxygen leaving blood through the blood-vessel interface is strongly diffusion dominated. It is commonly expressed in units of ml O_2 min^{-1} cm^{-2} mmHg^{-1}, and follows Fick's law $j_{tv} = -\alpha\nabla P$ at the interface. In single capillary models, the concentration distribution of oxygen is described by advection-diffusion partial differential equations in three dimensions. Thus the expression $-\alpha\nabla P$ yields the oxygen flux at any point in space. However, in large scale network models it is too expensive to compute all microscopic details of the oxygen distribution. Therefore an effective mass transfer coefficient (MTC) γ, similar to L_p of eq. (6), is used to obtain the transvascular flux density j_{tv} from average tissue and blood oxygen partial pressures [102] according to

$$j_{tv} = \gamma(P_v - P_t), \tag{10}$$

where P_t is the partial pressure of oxygen at the inner wall of the vessel lumen, and P_v is the partial pressure at the center of the vessel. Note that γ represents an effective radial diffusion coefficient of oxygen in blood. L_p of the Starling equation, on the other hand, represents the permeability of the wall. In small vessels, blood tends to form an RBC-rich core and a RBC-free boundary layer. For larger vessels ($r > 100\,\mu$m), the discrete nature of RBCs plays a lesser role. Therefore the MTC is function of the vessel radius r, hematocrit H, and blood oxygen saturation S [101].

The functional dependency $\gamma(r, H, S)$ can be obtained from single capillary simulations and experiments. Assuming radial symmetry, and further assuming that radial variations of the oxygen concentration in blood are negligible, the change of the oxygen flux along the vessel axis is simply given by the differential equation

$$q\frac{\mathrm{d}c}{\mathrm{d}x} = -2\pi r j_{tv}, \tag{11}$$

where q is the blood flow rate, and x denotes the longitudinal space coordinate on the vessel axis. In order to determine the oxygen distribution across an entire network, assumptions must be made on the distribution at vessel junctions, *e.g.* instant equilibration of the partial pressure of oxygen flowing into a junction. With the help of mass balance equations, the concentration of outflowing oxygen can be computed. Thus the solution for the oxygen concentration can be propagated downstream. We describe this in more detail in [41].

Furthermore, the tissue oxygen concentration $c_t = \alpha_t P_t$ is determined by the diffusion equation for the partial pressure P_t

$$0 = \alpha_t D\nabla^2 P_t - M(P_t) + J_{tv}, \tag{12}$$

where D is the diffusion coefficient of oxygen, $M(P)$ is a partial pressure dependent consumption rate, and J_{tv} is the source and drain strength distribution of vessels. J_{tv} can be formulated with the help of the Dirac δ distribution in analogy to (7). A general good approximation to the consumption rate of oxygen $M(P)$ is the well-known Michaelis-Menten relation

$$M(P) = M_0 \frac{P}{P + P'_{50}}, \tag{13}$$

which tends to zero for small P, assumes the value $M_0/2$ for $P = P'_{50}$ and goes asymptotically to the maximal consumption rate M_0. For some problems like tumor oxygenation it is usually assumed that the oxygen concentration rather low, *i.e.* $P_t < P'_{50}$. Then it is sufficient to use a linear approximation $M(P) \approx -\lambda P$ for some rate coefficient λ. In physiological conditions, $M(P)$ is often approximated by zero order kinetics $M(P) \approx M_0$. This is only applicable in case of good oxygenation since the solution for P_t can otherwise drop below zero.

The system of combined equations for the concentration of intravascular oxygen and tissue oxygen is very challenging to solve and it can only be done numerically. In [107, 109, 115] a Green's function method was used that is based on the Green's function G of the Laplacian ∇^2, where G is the solution to $\nabla^2 G(\mathbf{x}) = \delta(\mathbf{x})$. The solution to eq. (12) is thus formally given by the convolution of G with $M(P_t) + J_{tv}$ [109]. Goldman, in ref. [102], and the authors in the references therein use very fine grid tesselations of $3\,\mu\mathrm{m}$, and consider vessels as sources of oxygen with non-zero radius. This facilitates the numerical treatment of the transvascular flux coupling with help of the gradient boundary condition $-\alpha\nabla P_t = j_{tv}$ at vessel surfaces. We further explored the concepts used in our IFF paper [40] and followed [91, 109, 116] in the development of a new method to compute intra-and extravascular oxygen distributions [117]. Methods developed for the study of oxygen distributions can also be employed to consider distribution of other substances like drugs. Moreover oxygen adds the complication of hemoglobin binding which leads to nonlinear systems of equations. For other substances this can be omitted and linear equations are obtained. As aforementioned, in many cases it may be adequate to consider constant intravascular concentrations.

5.1 Simulation of oxygen distribution in tumors

Extremely good perfusion of tumor vessels cannot be assumed for tumors in general. This necessitates consideration of spatially varying substance concentrations because a substantial fraction may be lost during the transit through the tumor. The computational method developed in [41] and described above attempts to solve this problem for oxygen concentration distributions on macroscopic scales by solution of coupled systems of differential equations for intravascular and extravascular oxygen transport and diffusion to obtain a self-consistent numerical solution. This is computationally very expensive, however, this expense is justified since few simplifying assumptions need to be made for the vascular network and blood flow.

Maps of tissue oxygen partial pressure (PO_2) distributions emerging for various vascular networks and tissues were calculated previously according to the mathematical description of oxygen transport ([102, 109] and references therein). Results obtained in [41] for large synthetic tumor blood vessel networks, constructed along the lines sketched before, are shown in fig. 11. The numerical solution of [41] is a compromise between computational demand and presumably more accurate methods [102, 109]. The method allows computation of oxygenation in simulation boxes of ca. $0.5\,\mathrm{cm}^3$ on standard hardware (i7-2600K, 3.4 GHz, 4 GB Ram) within an hour. This was by far not achievable with the Green's function based method [109]. However, our method suffers from sub-linear convergence with the numerical grid constant h, *i.e.* the results depend strongly on the fineness of the discretization [41]. For a small artificial vasculature we obtained good qualitative agreement with the Green's function method but the computed PO_2 differs up to 10% of the value at the inlet. In spite of that, we obtain good agreement with experimentally data of normal breast tissue, and use the method to analyze oxygenation of breast tumors (see below).
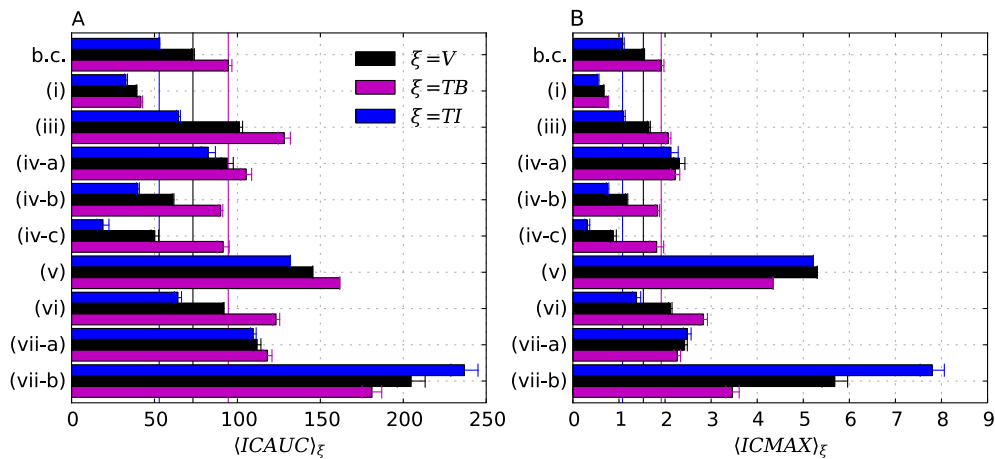
Fig. 11. Comparison of the mean values of drug doses for different cases and parameter variations. The quantities ICMAX and ICAUC are the local maximal drug concentration taken over time and the local time integral of the concentration (area under curve). We first computed the averages taken over different spatial regions, indexed by ξ, and then again averaged over a cohort of 15 simulated tumors. These regions are the viable tumor mass (V), a band behind the tumor boundary extending a $250\,\mu$m into the tumor (TB), and the adjacent tumor interior (TI), including necrotic and viable tumor. Error bars show standard deviations taken over the cohort of tumors. The meaning of the case labels is as follows: (b.c.) base case, (i) heavier drug particles, *i.e.* molecular mass increased by a factor of $2 \cdot 10^3$. (iii) neglected interstitial convection, (iv) tumor vascular permeability scaled by a factor of 10 (a), 1/10 (b), and 1/100 (c), (v) hydraulic conductivity of interstitium scaled by a factor of 10, (vi) number of normal lymphatics scaled by a factor of 10, (vii) number of tumor lymphatic equals 10% (a) and 100% (b) of the number of normal lymphatics. (Reprinted from [40]. © 2013, Welter and Rieger.)

Critical to performance and accuracy is the regularization of the singular source term $2\pi r j_{tv}$ of the tissue O$_2$ diffusion equation, containing Dirac δ distributions, in conjunction with an efficient numerical scheme for the solution of the diffusion equation. In general the method should yield a sparse system matrix to enable numerical solutions in $O(n \log n)$ time in the number of unknowns n. Moreover, the method should allow for coarse grid constants h of 5 to $30\,\mu$m to keep the number of unknowns low and simultaneously resolve O$_2$ concentration gradients around tumor vessels. In [90], optimal convergence was achieved by adaptive tesselation of the tissue domain, *i.e.* the discretization becomes more fine grained near singular source terms (blood vessels).

Our numerical scheme was applied in [41] to the case of breast tumors for which several groups measured hemoglobin concentrations c_{Hb} and average blood oxygen saturations Y in large cohorts of patients [118–121]. The oxygen partial pressure PO$_2$, the oxygen saturation and the hematocrit distribution computed in [41] for a synthetic blood vessel network are shown in fig. 12A, B, and C, respectively. The average saturation Y within these tumors can be above or below the saturation measured within healthy tissue. Moreover, saturations Y are high when the hemoglobin concentration c_{Hb} is also high, but tumors exhibiting low c_{Hb} exhibit broader ranges of saturations Y. In the base case (BASE), the use of different initial ($t = 0$) root node configurations (RC1 through RC9) leads to a spread in tumor oxygen saturations, but it does not predict the experimentally observed dependency of $Y(tumor)$ *versus* $Y(normal)$ since predicted $Y(tumor)$ is always larger than $Y(normal)$ [41]. Therefore we considered a phenomenological *ad hoc* extension of the model by vaso-compression, *i.e.* essentially a reduction of the radii of arterioles and venules. This leads to good agreement with mammography data (case CMPR) [41]. The reason for this is the reduction of blood flow, thus draining a greater fraction of the supplied O$_2$ in order to meet metabolic demand. The variation of hemoglobin concentrations c_{Hb} can be explained by variations of the emerging vascular volume in tumors. Assuming that high vascular volumes imply elevated flow rates, a lower variance of Y for such tumors is explained by these elevated flow rates which drive Y to nearly full saturation. This also means that other variables, *e.g.* tissue PO$_2$, have a diminished effect on the obtained Y. Thus, rather subtle variations in arterial radii can lead to large blood flow variations, in addition to fluctuations introduced by varying initial networks of the host. The experimental data might imply that tumor vascular networks that exhibit higher saturations than normal are vastly different in their vascular architecture than networks that exhibit low saturations. However, our simulations suggest that these networks nevertheless share the traits of typical tumor vascular networks, *i.e.* as outlined in the introduction and sect. 3.

It is standard for tumor growth models to assume a constant vascular PO$_2$. By definition, this approximation does not explain variation of saturations Y in the cohort of patients, since then Y becomes an input parameter. In comparison with the full model, the constant-PO$_2$ approximation over-predicts PO$_2$ in the neo-vascular plexus around the tumor periphery, and it fails to predict local oxygen depletion in vessels threading the tumor center (see fig. 12D). This should be taken into account in applications like therapy planing and other pharmacokinetical studies, or else, the efficacy of the therapy might be overestimated.
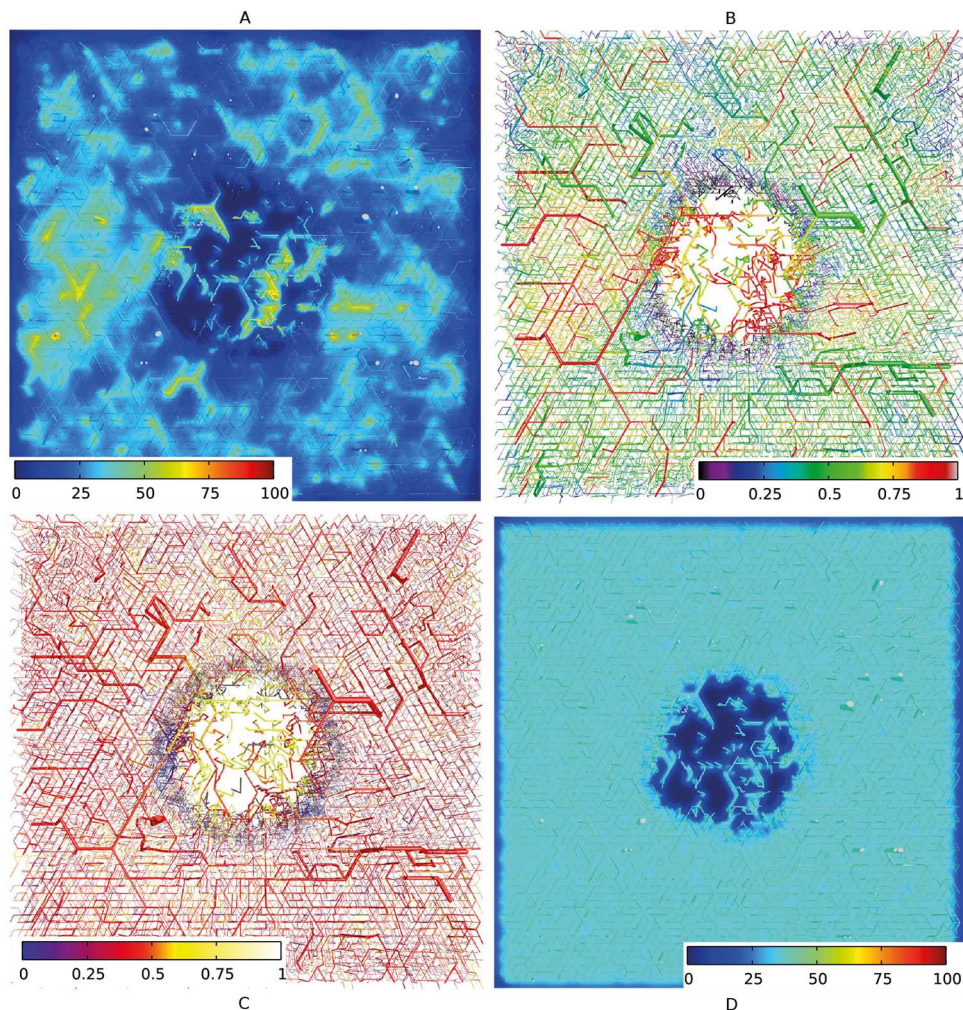
Fig. 12. Blood oxygen saturation and oxygen partial pressure. The top row (A,B) shows the intra-and extravascular partial pressure of oxygen P, and P_t, respectively. (C) shows the hematocrit distribution within the same network. (D) shows the oxygen partial pressure obtained from a simplified model where the intra-vascular oxygen partial pressure was held constant. The data were computed for artificial vascular networks obtained from simulations of tumor growth and vascular remodeling [41]. A spherical region of approximately 2 mm radius was changed by the tumor. The partial pressure in tissue P_t is shown in a slice through the center of the simulation domain. The camera is looking vertically onto the cutting plane so that the whole lateral extent of 8 mm is shown. The vessel network is visualized as a collection of cylinders that have been truncated 100 μm above and below the central plane. Vascular cross sections appearing at the lower and upper faces of the slab and generated by truncation are light gray. In (B) and (C), only the network is shown.

Previously, Secomb's Greensfunction method [107] was used to study oxygen concentration distributions in microscopic tissue sections using blood vessel networks of tumors obtained from animal models [109] as well as in theoretical idealizations of the vasculature of the human brain [113, 115]. The finite difference method by [108] was used in several publications [102, 114, and the refs. therein] to study oxygen concentrations in capillary networks of muscle fibers. There are several other papers in which specifically the oxygen distribution in tumors is considered [85–89, 122–124]. However, in these works, the vasculature is represented by extremely simplified idealizations, *i.e.* by arrays of disjoint, often parallel, capillaries. The vascular oxygen saturation (or partial pressure) is an input parameter in these models and the macroscopic compartmentalization of the tumor vasculature is neglected. Therefore, such models are more suited to determine precise statistical frequency distributions of oxygen concentration levels in tissue, given a specific microvascular density and blood oxygen concentration.

6 Predictions and outlook

To indicate the current status of quantitative theoretical models for the tumor vasculature we have compared the predictions of the model developed in [40, 41] for various quantities characterizing microvasculature, blood flow, IFF, and oxgen distribution with (some) available experimental data in table I of the Supplementary Material. The parameters used in the model are summarized in table II of the Supplementary Material again together with experimental

estimates. The agreement is quite promising, with a few exceptions. For instance the model predicts regional blood flow rBF that is about a factor of 5 to 10 above measured data from breast tumors. This failure might also be due to the size of the considered tumors (4 mm in diameter, simulated, *versus* centimeter sized real tumors). [125] showed that blood flow rBF of experimental tumors (2–0.3 ml/g/min) correlates negatively with size (0.1–10 cm^3 tumor volume), consistent with our results. The reasons for this size dependency are currently unknown. However, it suggests that vasculatures can only provide a fixed blood flow per surface area. Hence rBF would decrease with decreasing surface to volume ratio of the tumor spheroid.

A major limitation of the model in [41] is the restricted applicability to only well perfused tumors. The prediction of good perfusion is inherent to this model of vascular remodeling since tumor vessels can only dilate, not shrink, and surviving vessels must route the blood volume coming from the surrounding vasculature. Therefore it would be worthwhile to explore biophysically motivated extensions to vascular dilation and regression processes rather than limiting blood flow by *ad hoc* shrinkage of arterial radii. One such possible extension already exists in the vascular adaptation model [126], variations of which are frequently used in other mathematical models of tumor growth. Essentially in this model a shrinking-tendency is balanced by a wall shear-stress–dependent growth signal.

Moreover, compression of blood vessels is insufficiently understood. Forces involved were studied quantitatively, separately, to some degree (see refs. below). Obviously, the deformation of vessel walls is governed by a balance of forces which are tensile and compressive stress within the vessel wall, blood pressure, interstitial fluid pressure, and solid pressure. Solid pressure compresses vessels [127–129] and there is evidence that an elevated IFP aids in compression of vessels [130, 131]. However, the interplay of these forces still seems somewhat elusive, and there is, to our knowledge, no predictive model of the response of the vessel wall that takes these factors into account. A physical consideration based on first principles *e.g.* with the help of a elasto-plastic mechanical model of vascular walls in combination with a mechanical model of tissue could help elucidate the forces involved and ultimately yield better predictions of blood flow. If, in future, tumors with low flow rates will be considered, models of blood flow, interstitial fluid flow and drug transport need to take into account the loss of blood plasma and intravascular concentration variations. Mathematically this could be treated in similar to the techniques used for the simulation of oxygen distributions in [41].

A number of results have been obtained by the studies within the modeling framework described in this review that appear to be robust against further model refinements. The characteristic compartmentalization of the tumor vasculature was already mentioned in the previous subsection. In [33] it was pointed out that the formation of the global morphology of the tumor vasculature is dominated by vessel collapse inside the tumor rather than angiogenic sprouting, which is restricted to the outer rim of the growing tumor. Consequently its (apparently) fractal nature is reminiscent of a flow correlated percolation process [33] rather than an invasion percolation as was hypothesized in [76, 132].

The formation of hot-spots, *i.e.* regions of drastically increased blood density within the tumor was shown to be related to regions with strong blood pressure gradients in the initial arterio-venous vasculature [39]. For shear force determined vessel collapse such a scenario is plausible, since between vessels with strongly different blood pressure a shunt generated by angiogenic sprouting will carry a strong blood flow and therefore collapse with a correspondingly reduced probability. Blood borne drug transport within the tumor is actually very efficient [67], in contrast to what is predicted by vessel-in-growth models [21, 22]. The reason is that badly perfused vessels collapse with increased probability which implies that predominantly well perfused tumor vessels will sustain.

Interstitial fluid pressure is generally increased in vascularized tumors but computer simulations of interstitial fluid flow in vascularized tumors within an arterio-venous initial network showed [40] that it cannot be a direct cause for impeded drug delivery, as was hypothesized in [7–9]. The model predicts that an increase of the permeability of vessel walls or tumor tissue or lymphatic walls will always increase interstitial fluid pressure but also the interstitial fluid flow and thus improves drug delivery via convective transport. The physical explanation is simply that it is misleading to consider the pressure drop along the vessel wall alone as the driving force for IFF —in principle the complete network of hydraulic resistors has to be taken into account to obtain reliable predictions. Similar results were later obtained with a related model using a grid-like initial vasculature [133].

A consequence of the simulations performed in [40] is that a tumor therapy aimed solely at reducing the vessel leakiness cannot be effective, implying that concepts like normalization of tumor vasculature [10] have intrinsic problems if they target for a reduction of vessel wall permeability (or hydraulic conductivity) alone. Only cases in which the tumor vessel walls are so leaky that they extravasate such a substantial amount of blood plasma (including drug) that leads to a drastic reduction of the downstream flux rate and thus blood borne drug concentration a decrease of wall permeability would improve tumor vessel perfusion and potentially drug delivery. This extreme case was studied in the highly simplified model presented in [99], which uses a percolation network as a representation of the tumor vasculature. It should be noted that the drug delivery improvement reported there is not a consequence of reducing the putative interstitial fluid pressure barrier [7–9] but simply a consequence of improved vessel perfusion in the central part of the assumed percolation network. It is questionable that comparable effects can be obtained in realistic tumor vasculature derived from arterio-venous networks and displaying the characteristic compartmentalization mentioned above. The simulation results of [40] also demonstrated that increasing the permeability of tumor tissue itself has the potential to improve drug delivery, supporting experimental observations reviewed in [95, 127].

The current state of *in silico* models of the dynamical evolution of tumor vasculature is still in the beginning and still far from the ultimate goal to gain a mechanistic understanding of vascular normalization or vessel growth promotion therapies and to become a patient-specific predictive tool to improve diagnosis, therapy planning and treatment of a tumor. We have sketched the basic components that an integrative model must necessarily have and showed that the few serious implementations of model frameworks that comprise all the sketched modules already produce non-trivial predictions that are in agreement with recent experimental data.

References

1. Rakesh K. Jain, Cancer Res. **48**, 2641 (1988).
2. Peter Vaupel, Friedrich Kallinowski, Paul Okunieff, Cancer Res. **49**, 6449 (1989).
3. Michael Hckel, Peter Vaupel, J. Natl. Cancer Inst. **93**, 266 (2001).
4. L.H. Gray, A.D. Conger, M. Ebert, S. Hornsey, O.C.A. Scott, Brit. J. Radiol. **26**, 638 (1953).
5. R.K. Jain, Cancer Res. **47**, 3039 (1987).
6. R.K. Jain, L.T. Baxter, Cancer Res. **48**, 7022 (1988).
7. R.K. Jain, Annu. Rev. Biomed. Eng. **1**, 241 (1999).
8. C.H. Heldin, K. Rubin, K. Pietras, A. Ostman, Nat. Rev. Cancer **4**, 806 (2004).
9. A.I. Minchinton, I.F. Tannock, Nat. Rev. Cancer **6**, 583 (2006).
10. R.K. Jain, Science **307**, 58 (2005).
11. Ricky T. Tong, Yves Boucher, Sergey V. Kozin, Frank Winkler, Daniel J. Hicklin, Rakesh K. Jain, Cancer Res. **64**, 3731 (2004).
12. Rakesh K. Jain, Cancer Cell **26**, 605 (2015).
13. Lee B. Rivera, Gabriele Bergers, Science **349**, 694 (2015).
14. Mary Purcell Wiedeman, Ronald F. Tuma, Harvey Norman Mayrovitz, *An Introduction to Microcirculation* (New York, Academic Press, 1981).
15. Cecil D Murray, Proc. Natl. Acad. Sci. U.S.A. **12**, 207 (1926).
16. T.F. Sherman, J. Gen. Physiol. **78**, 431 (1981).
17. Fan Yuan, Hassan A. Salehi, Yves Boucher, Usha S. Vasthare, Ronald F. Tuma, Rakesh K. Jain, Cancer Res. **54**, 4564 (1994).
18. E.N. Marieb, K. Hoehn, *Human Anatomy and Physiology* (Pearson, 2013).
19. A.R.A. Anderson, M.A.J. Chaplain, Bull. Math. Biol. **60**, 857 (1998).
20. M.A. Gimbrone, R.S. Cotran, S.B. Leapman, J. Folkman, J. Natl. Cancer Inst. **52**, 413 (1974).
21. S.R. McDougall, A.R.A. Anderson, M.A.J. Chaplain, J.A. Sherratt, Bull. Math. Biol. **64**, 673 (2002).
22. S.R. McDougall, A.R.A. Anderson, M.A.J. Chaplain, J. Theor. Biol. **241**, 564 (2006).
23. J. Wu, S. Xu, Q. Long, M.W. Collins, C.S. Konig, G. Zhao, Y. Jiang, A.R. Padhani, J. Biomech. **41**, 996 (2008).
24. Jie Wu, Quan Long, Shixiong Xu, Anwar R. Padhani, J. Biomech. **42**, 712 (2009).
25. B. Döme, S. Paku, B. Somlai, J. Tímár, J. Pathol. **197**, 355 (2002).
26. J. Holash, P.C. Maisonpierre, D. Compton, P. Boland, C.R. Alexander, D. Zagzag, G.D. Yancopoulos, S.J. Wiegand, Science **284**, 1994 (1999).
27. T. Alarcon, H.M. Byrne, P.K. Maini, J. Theor. Biol. **225**, 257 (2003).
28. Helen M. Byrne, Markus R. Owen, Tomas Alarcon, James Murphy, Philip K. Maini, Math. Mod. Meth. Appl. Sci. **16**, 1219 (2006).
29. M.R. Owen, T. Alarcn, P.K. Maini, H.M. Byrne, J. Math. Biol. **58**, 689 (2009).
30. R. Weislo, W. Dzwinel, D.A. Yuen, A.Z. Dudek, J. Mol. Model. **15**, 1517 (2009).
31. R. Betteridge, M.R. Owen, H.M. Byrne, T. Alarcon, P.K. Maini, Networks Heterogen. Media **1**, 515 (2006).
32. Katalin Bartha, Heiko Rieger, J. Theor. Biol. **241**, 903 (2006).
33. D.S. Lee, H. Rieger, K. Bartha, Phys. Rev. Lett. **96**, 058104 (2006).
34. Min Wu, Hermann B. Frieboes, Steven R. McDougall, Mark A.J. Chaplain, Vittorio Cristini, John Lowengrub, J. Theor. Biol. **320**, 131 (2013).
35. J.L. Gevertz, Comput. Math. Methods Med. **2011**, 830515 (2011).
36. N. Safaeian, *Computational Modelling of Capillaries in Neuro-vascular Coupling: A Thesis Presented for the Degree of Doctor of Philosophy in Mechanical Engineering at the University of Canterbury, Christchurch, New Zealand* (University of Canterbury, 2012).
37. W. Schreiner, J. Biomed. Eng. **15**, 148 (1993).
38. Ralf Gödde, Haymo Kurz, Dev. Dyn. **220**, 387 (2001).
39. M. Welter, K. Bartha, H. Rieger, J. Theor. Biol. **259**, 405 (2009).
40. M. Welter, H. Rieger, PLoS ONE **8**, e70395 (2013).
41. M. Welter, T. Fredrich, H. Rinneberg, H. Rieger, Relation between tumor oxygenation, vascular remodeling, and blood flow: a computational model with applications to breast cancer, submitted to PLOS Comp. Biol. (2015).

42. F. Cassot, F. Lauwers, C. Fouard, S. Prohaska, V. Lauwers-Cances, Microcirculation **13**, 1 (2006).
43. Spyros K. Stamatelos, Eugene Kim, Arvind P. Pathak, Aleksander S. Popel, Microvasc. Res. **91**, 8 (2014).
44. Romain Guibert, Caroline Fonta, Franck Plouraboue, J. Cereb. Blood Flow Metab. **30**, 1860 (2010).
45. J. Lee, P. Beighley, E. Ritman, N. Smith, Med. Image Anal. **11**, 630 (2007).
46. A.R. Pries, T.W. Secomb, T. Gessner, M.B. Sperandio, J.F. Gross, P. Gaehtgens, Circ. Res. **75**, 904 (1994).
47. A.R. Pries, T.W. Secomb, Am. J. Physiol. - Heart Circulat. Physiol. **289**, H2657 (2005).
48. A.R. Pries, T.W. Secomb, P. Gaehtgens, J.F. Gross, Circ. Res. **67**, 826 (1990).
49. N. Safaeian, M. Sellier, T. David, J. Theor. Biol. **271**, 145 (2011).
50. A.R. Pries, T.W. Secomb, P. Gaehtgens, J.F. Gross, Circ. Res. **67**, 826 (1990).
51. Peter Carmeliet, Rakesh Jain, Nature **407**, 249 (2000).
52. Peter Carmeliet, Rakesh K. Jain, Nature **473**, 298 (2011).
53. J. Holash, S.J. Wiegand, G.D. Yancopoulos, Oncogene **18**, 5356 (1999).
54. B. Döme, M. Hendrix, S. Paku, J. Tóvarí, Am. J. Path. **170**, 1 (2007).
55. R. Erber, U. Eichelsbacher, V. Powajbo, T. Korn, V. Djonov, J. Lin, H.-P. Hammes, R. Grobholz, A. Ullrich, P. Vajkoczy, EMBO **25**, 628 (2006).
56. M. Scianna, C.G. Bell, L. Preziosi, J. Theor. Biol. **333**, 174 (2013).
57. Elizabeth A. Logsdon, Stacey D. Finley, Aleksander S. Popel, Feilim Mac Gabhann, J. Cell. Molec. Med. **18**, 1491 (2014).
58. C.J. Breward, H.M. Byrne, C.E. Lewis, Bull. Math. Biol. **65**, 609 (2003).
59. R.P. Araujo, D.L.S. McElwain, J. Math. Biol. **66**, 1039 (2004).
60. N. Bellomo, E. De Angelis, L. Preziosi, J. Theor. Med. **5**, 111 (2003).
61. T. Alarcn, M.R. Owen, H.M. Byrne, P.K. Maini, Comp. Math. Methods Med. **7**, 85 (2006).
62. A. Stephanou, S.R. McDougall, A.R.A. Anderson, M.A.J. Chaplain, Math. Comput. Modell. **41**, 1137 (2005) Modelling Complex Systems in Molecular Biology and Tumor Dynamics and Control.
63. A. Stephanou, S.R. McDougall, A.R.A. Anderson, M.A.J. Chaplain, Math. Comput. Model. **44**, 96 (2006).
64. M.A.J. Chaplain, S.R. McDougall, A.R.A. Anderson, Annu. Rev. Biomed. Eng. **8**, 233 (2006).
65. Yan Cai, Shixiong Xu, Jie Wu, Quan Long, J. Theor. Biol. **279**, 90 (2011).
66. Michael A. Gimbrone, Ramzi S. Cotran, Stephen B. Leapman, Judah Folkman, J. Natl. Cancer Inst. **52**, 413 (1974).
67. M. Welter, H. Rieger, Eur. Phys. J. E **33**, 149 (2010).
68. P. Tracqui, Rep. Prog. Phys. **72**, 056701 (2009).
69. Katie Bentley, Holger Gerhardt, Paul A. Bates, J. Theor. Biol. **250**, 25 (2008).
70. Holger Gerhardt, Matthew Golding, Marcus Fruttinger, Christina Ruhrberg, Andrea Lundkvist, Alexandra Abramsson, Michael Jeltsch, Christopher Mitchell, Kari Alitalo, David Shima, Christer Betsholz, J. Cell Biol. **161**, 1163 (2003).
71. A.R. Pries, T.W. Secomb, P. Gaehtgens, Am. J. Physiol. **275**, H349 (1994).
72. M. Welter, K. Bartha, H. Rieger, J. Theor. Biol. **250**, 257 (2008).
73. Axel R. Pries, Michael Höpfner, Ferdinand le Noble, Mark W. Dewhirst, Timothy W. Secomb, Nat. Rev. Cancer **10**, 587 (2010).
74. H. Perfahl, H.M. Byrne, T. Chen, V. Estrella, T. Alarcon, A. Lapin, R.A. Gatenby, R.J. Gillies, M.C. Lloyd, P.K. Maini, M. Reuss, M.R. Owen, PLoS ONE **6**, e14790 (2011).
75. J. Du, F.H. Li, H. Fang, J.G. Xia, C.X. Zhu, J. Ultrasound Med. **27**, 833 (2008).
76. Yuval Gazit, David A. Berk, Laurence T. Baxter Michael Leunig, Rakesh K. Jain, Phys. Rev. Lett. **75**, 2428 (1995).
77. Alessandro Taloni, Martine Ben Amar, Stefano Zapperi, Caterina A.M. La Porta, Eur. Phys. J. Plus **130**, 224 (2015).
78. R.K. Jain, R.T. Tong, L.L. Munn, Cancer Res. **67**, 2729 (2007).
79. J. Zhao, H. Salmon, M. Sarntinoranont, Microvasc. Res. **73**, 224 (2007).
80. M. Sefidgar, M. Soltani, K. Raahemifar, H. Bazmara, S.M. Nayinian, M. Bazargan, J. Biol. Eng **8**, 12 (2014).
81. M. Sefidgar, M. Soltani, K. Raahemifar, M. Sadeghi, H. Bazmara, M. Bazargan, M. Mousavi Naeenian, Microvasc. Res. **99**, 43 (2015).
82. P. Knabner, L. Angermann, *Numerik partieller Differentialgleichungen* (Springer Verlag, 2000).
83. S.M. Wise, J.S. Lowengrub, H.B. Frieboes, V. Cristini, J. Theor. Biol. **253**, 524 (2008).
84. J.P. Sinek, S. Sanga, X. Zheng, H.B. Frieboes, M. Ferrari, V. Cristini, J. Math. Biol. **58**, 485 (2009).
85. A. Daşu, I. Toma-Daşu, M. Karlsson, Phys. Med. Biol. **48**, 2829 (2003).
86. C.J. Kelly, M. Brady, Phys. Med. Biol. **51**, 5859 (2006).
87. D. Monnich, E.G. Troost, J.H. Kaanders, W.J. Oyen, M. Alber, D. Thorwarth, Phys. Med. Biol. **56**, 2045 (2011).
88. A.C. Skeldon, G. Chaffey, D.J. Lloyd, V. Mohan, D.A. Bradley, A. Nisbet, PLoS ONE **7**, e38597 (2012).
89. I. Espinoza, P. Peschke, C.P. Karger, Med. Phys. **40**, 081703 (2013).
90. Carlo D'Angelo, SIAM J. Numer. Anal. **50**, 194 (2012).
91. L. Cattaneo, P. Zunino, Int. J. Numer. Method Biomed. Eng. **30**, 1347 (2014).
92. R.K. Jain, T. Stylianopoulos, Nat. Rev. Clin. Oncol. **7**, 653 (2010).
93. A.J. Primeau, A. Rendon, D. Hedley, L. Lilge, I.F. Tannock, Clin. Cancer Res. **11**, 8782 (2005).
94. J.H. Zheng, C.T. Chen, J.L. Au, M.G. Wientjes, AAPS PharmSci. **3**, E15 (2001).
95. R.K. Jain, J. Clin. Oncol. **31**, 2205 (2013).
96. P.A. Netti, D.A. Berk, M.A. Swartz, A.J. Grodzinsky, R.K. Jain, Cancer Res. **60**, 2497 (2000).
97. Trevor D. McKee, Paola Grandi, Wilson Mok, George Alexandrakis, Numpon Insin, John P. Zimmer, Moungi G. Bawendi, Yves Boucher, Xandra O. Breakefield, Rakesh K. Jain, Cancer Res. **66**, 2509 (2006).

98. Benjamin Diop-Frimpong, Vikash P. Chauhan, Stephen Krane, Yves Boucher, Rakesh K. Jain, Proc. Natl. Acad. Sci. U.S.A. **108**, 2909 (2011).
99. Triantafyllos Stylianopoulos, Rakesh K. Jain, Proc. Natl. Acad. Sci. U.S.A. **110**, 18632 (2013).
100. A.C. Shieh, M.A. Swartz, Phys. Biol. **8**, 015012 (2011).
101. J.D. Hellums, P.K. Nair, N.S. Huang, N. Ohshima, Ann. Biomed. Eng. **24**, 1 (1996).
102. D. Goldman, Microcirculation **15**, 795 (2008).
103. A. Krogh, J. Physiol. (London) **52**, 409 (1919).
104. P.K. Nair, J.D. Hellums, J.S. Olson, Microvasc. Res. **38**, 269 (1989).
105. P.K. Nair, N.S. Huang, J.D. Hellums, J.S. Olson, Microvasc. Res. **39**, 203 (1990).
106. T.E. Moschandreou, C.G. Ellis, D. Goldman, Math. Biosci. **232**, 1 (2011).
107. Richard Hsu, Timothy W. Secomb, Math. Biosci. **96**, 61 (1989).
108. D. Goldman, A.S. Popel, J. Theor. Biol. **206**, 181 (2000).
109. Timothy W. Secomb, Richard Hsu, Eric Y.H. Park, Mark W. Dewhirst, Ann. Biomed. Eng. **32**, 1519 (2004).
110. D. Goldman, R.M. Bateman, C.G. Ellis, Am. J. Physiol. Heart Circ. Physiol. **287**, H2535 (2004).
111. D. Goldman, R.M. Bateman, C.G. Ellis, Am. J. Physiol. Heart Circ. Physiol. **290**, H2277 (2006).
112. N.M. Tsoukias, D. Goldman, A. Vadapalli, R.N. Pittman, A.S. Popel, J. Theor. Biol. **248**, 657 (2007).
113. N. Safaeian, M. Sellier, T. David, J. Theor. Biol. **271**, 145 (2011).
114. G.M. Fraser, D. Goldman, C.G. Ellis, Microcirculation **20**, 748 (2013).
115. N. Safaeian, T. David, J. Cereb. Blood Flow Metab. **33**, 1633 (2013).
116. D.A. Beard, Ann. Biomed. Eng. **29**, 837 (2001).
117. Heiko Rieger, Michael Welter, WIREs Syst. Biol. Med. **7**, 113 (2015).
118. D. Grosenick, K.T. Moesta, M. Moller, J. Mucke, H. Wabnitz, B. Gebauer, C. Stroszczynski, B. Wassermann, P.M. Schlag, H. Rinneberg, Phys. Med. Biol. **50**, 2429 (2005).
119. L. Spinelli, A. Torricelli, A. Pifferi, P. Taroni, G. Danesini, R. Cubeddu, Phys. Med. Biol. **50**, 2489 (2005).
120. P. Taroni, A. Torricelli, L. Spinelli, A. Pifferi, F. Arpaia, G. Danesini, R. Cubeddu, Phys. Med. Biol. **50**, 2469 (2005).
121. P. Taroni, Photochem. Photobiol. Sci. **11**, 241 (2012).
122. P. Degond, S. Mas-Gallic, Math. Comput. **53**, 485 (1989).
123. J.H. Lagerlf, J. Kindblom, E. Cortez, K. Pietras, P. Bernhardt, Med. Phys. **40**, 024101 (2013).
124. J.H. Lagerlf, J. Kindblom, P. Bernhardt, Med. Phys. **41**, 044101 (2014).
125. F. Kallinowski, K.H. Schlenger, M. Kloes, M. Stohrer, P. Vaupel, Int. J. Cancer **44**, 266 (1989).
126. A.R. Pries, B. Reglin, T.W. Secomb, Hypertension **46**, 725 (2005).
127. V.P. Chauhan, J.D. Martin, H. Liu, D.A. Lacorre, S.R. Jain, S.V. Kozin, T. Stylianopoulos, A.S. Mousa, X. Han, P. Adstamongkonkul, Z. Popovi?, P. Huang, M.G. Bawendi, Y. Boucher, R.K. Jain, Nat. Commun. **4**, 2516 (2013).
128. T. Stylianopoulos, J.D. Martin, V.P. Chauhan, S.R. Jain, B. Diop-Frimpong, N. Bardeesy, B.L. Smith, C.R. Ferrone, F.J. Hornicek, Y. Boucher, L.L. Munn, R.K. Jain, Proc. Natl. Acad. Sci. U.S.A. **109**, 15101 (2012).
129. V.P. Chauhan, Y. Boucher, C.R. Ferrone, S. Roberge, J.D. Martin, T. Stylianopoulos, N. Bardeesy, R.A. DePinho, T.P. Padera, L.L. Munn, R.K. Jain, Cancer Cell **26**, 14 (2014).
130. G. Griffon-Etienne, Y. Boucher, C. Brekken, H.D. Suit, R.K. Jain, Cancer Res. **59**, 3776 (1999).
131. K.E. DelGiorno, M.A. Carlson, R. Osgood, P.P. Provenzano, J.S. Brockenbough, C.B. Thompson, H.M. Shepard, G.I. Frost, J.D. Potter, S.R. Hingorani, Cancer Cell **26**, 16 (2014).
132. J.W. Baish, R.K. Jain, Nat. Med. **4**, 984 (1998).
133. Min Wu, Hermann B. Frieboes, Mark A.J. Chaplain, Steven R. McDougall, Vittorio Cristini, John S. Lowengrub, J. Theor. Biol. **355**, 194 (2014).
134. J.W. Baish, T. Stylianopoulos, R.M. Lanning, W.S. Kamoun, D. Fukumura, L.L. Munn, R.K. Jain, Proc. Natl. Acad. Sci. U.S.A. **108**, 1799 (2011).